Mapping the spatial distribution of NO_2 with in situ and remote sensing instruments during the Munich NO_2 imaging campaign

Gerrit Kuhlmann[1], Ka Lok Chan[2,3,*], Sebastian Donner[4], Ying Zhu[2], Marc Schwaerzel[1], Steffen Dörner[4], Jia Chen[5], Andreas Hueni[6], Duc Hai Nguyen[5,+], Alexander Damm[6,7], Annette Schütt[2], Florian Dietrich[5], Dominik Brunner[1], Cheng Liu[8], Brigitte Buchmann[1], Thomas Wagner[4], and Mark Wenig[2]

[1]Swiss Federal Laboratories for Materials Science and Technology (Empa), Dübendorf, Switzerland
[2]Meteorological Institute, Ludwig-Maximillians-University (LMU), Munich, Germany
[3]Remote Sensing Technology Institute (IMF), German Aerospace Center (DLR), Oberpfaffenhofen, Germany
[4]Max Planck Institute for Chemistry (MPIC), Mainz, Germany
[5]Environmental Sensing and Modeling, Technical University of Munich (TUM), Munich, Germany
[6]Department of Geography, University of Zurich (UZH), Zurich, Switzerland
[7]Swiss Federal Institute of Aquatic Science and Technology (Eawag), Dübendorf, Switzerland
[8]Department of Precision Machinery and Precision Instrumentation, University of Science and Technology of China (USTC), Hefei, China
[*]now at: Rutherford Appleton Laboratory Space, Harwell Oxford, United Kingdom
[+]now at: Leibniz Supercomputing Centre (LRZ), Garching bei München, Germany

Correspondence: Gerrit Kuhlmann (gerrit.kuhlmann@empa.ch)

Abstract. We present results from the Munich Nitrogen dioxide (NO_2) Imaging Campaign (MuNIC) where NO_2 near-surface concentrations (NSC) and vertical column densities (VCD) were measured with stationary, mobile and airborne in situ and remote sensing instruments in Munich, Germany. The most intensive day of the campaign was 7 July 2016, when the NO_2 VCD field was mapped with the Airborne Prism Experiment (APEX) imaging spectrometer. The spatial distribution of APEX VCDs was rather smooth with a horizontal gradient between lower values upwind and higher values downwind of the city center. The NO_2 map had no pronounced source signatures except for the plumes of two combined heat and power plants (CHP). The APEX VCDs have a fair correlation with mobile MAX-DOAS observations from two vehicles conducted in the same afternoon (r = 0.55). In contrast to the VCDs, mobile NSC measurements revealed high spatial and temporal variability along the roads with highest values in congested areas and tunnels. The NO_x emissions of the two CHP plants were estimated from the APEX observations using a mass-balance approach. The NO_x emission estimates are consistent with CO_2 emissions determined from two ground-based FTIR instruments operated near one CHP plant. The estimates are higher than the reported emissions but probably overestimated because the uncertainties are large, as conditions were unstable and convective with low and highly variable wind speeds. Under such conditions, the application of mass balance approaches is problematic because they assume steady-state conditions. We conclude that airborne imaging spectrometers are well suited to map the spatial distribution of NO_2 VCDs over large areas. The emission plumes of point sources can be detected in the APEX observations, but accurate flow fields are essential to estimate emissions with sufficient accuracy. The application of airborne imaging spectrometers for studying NSCs is less straight forward and requires to account for the non-trivial relationship between VCDs and NSCs.

1 Introduction

20 Nitrogen oxides (NO_x = NO + NO_2) are important precursors of ozone and particulate matter and thus play an important role in the formation of photochemical smog. Except close to source, NO_2 is usually the dominant component of NO_x and is also the more critical species in terms of health effects (Beelen et al., 2014; Brunekreef and Holgate, 2002). Because of their negative effects on health, NO_2 concentration levels are limited by air pollution legislation, but these limits are still frequently exceeded in urban areas (European Environment Agency, 2019; World Health Organization, 2021). NO_x is mainly emitted

25 by road traffic but also by residential heating, industrial facilities, power plants and some other combustion sources. Because of these localized emissions and the relative short lifetime of NO_2, NO_2 concentrations have a high spatial and temporal variability making high-resolution NO_2 maps an important tool for urban air pollution control and epidemiological studies (Maiheu et al., 2017).

   NO_2 maps can be created in different ways each having its specific advantages and disadvantages: In situ ground measure-

30 ments can be combined with geostatistical methods such as land-use-regression models to generate city-wide air pollution maps (e.g., Mueller et al., 2015) but urban air quality monitoring networks are typically very sparse, limiting the accuracy of such maps, although mobile sensors on public buses or trams could increase the measurement density (e.g., Hagemann et al., 2014; Hundt et al., 2018). Dense networks of low-cost sensors have also been proposed as a complement to the traditional networks, but issues with precision, stability or specificity of existing sensors remain an obstacle for their widespread deploy-

35 ment (Heimann et al., 2015; Bigi et al., 2018; Karagulian et al., 2019). As an alternative, networks of ground-based remote sensing instruments including multi-axis differential optical absorption spectroscopy (MAX-DOAS) (Leigh et al., 2007) and tomographic long-path (LP) DOAS systems (Platt et al., 2009) can be used to retrieve NO_2 maps. The disadvantage of this method is that a high spatial resolution can only be achieved with a very large number of light paths making a city-wide network expensive. Furthermore, the resulting NO_2 maps are mainly representing concentrations above buildings and not near the

40 ground. A third option is the use of imaging spectrometers on satellites and aircraft. Current satellite instruments have spatial resolutions down to a few kilometers, which is still too coarse for resolving NO_2 in a city. However, satellite instruments have been shown to be capable of observing the downwind plume of large cities (e.g., Beirle et al., 2011, 2019; Lorente et al., 2019). In contrast, airborne imaging spectrometers have inherently much higher spatial resolutions of a few tens of meters and thus can retrieve detailed NO_2 maps for whole cities (Heue et al., 2008; Lawrence et al., 2015; Popp et al., 2012; Schönhardt

45 et al., 2015; Tack et al., 2017; Nowlan et al., 2016; Tack et al., 2019). However, satellite and airborne instruments measure (tropospheric) vertical columns densities (VCD), while near-surface concentrations (NSC) is the quantity of interest for the assessment of air pollution exposure. Since the linkage between VCDs and NSCs is variable and depends on various factors (e.g., topography, emission sources and meteorological data), algorithms have been developed to transfer VCDs to NSCs for satellite observations using statistical models trained with NO_2 monitoring networks (e.g. Xu et al.; de Hoogh et al., 2019;

50 Kim et al., 2021).

These algorithms require large training datasets and cannot be applied to airborne measurement campaigns as typical urban monitoring networks are too small to train the relationship between VCDs and NSCs from a single measurement flight. This limits the current capacity to reliably retrieve NSCs and to study the spatial variability of NO_2 and its sources in cities with airborne remote sensing observations. We therefore conducted the Munich NO_2 Imaging Campaign (MuNIC) to validate airborne imaging spectrometers with ground-based observations and to collect data for advancing the understanding on the relationship between VCDs and NSCs in Munich, Germany. We collected data with the Airborne Prism EXperiment (APEX) imaging spectrometer (Schaepman et al., 2015) and measured NO_2 VCDs and NSCs using mobile (MAX-DOAS, CAPS, CE-DOAS) and stationary instruments (LP-DOAS, MAX-DOAS) as well as meteorological and other related parameters. In this paper, we validate the APEX NO_2 map using the mobile MAX-DOAS observations, analysis the consistency and relationship between NO_2 VCDs and NSCs, and demonstrate the applicability of the collected data to estimate the emissions of the two largest point sources in the city.

2 Data and method

The MuNIC campaign was conducted from 1-13 July 2016 in Munich, Germany (48.1375°N, 11.575°E) measuring NO_2 NSCs and VCDs with stationary, mobile and airborne instruments (Fig. 1; Tab. 1). The most intensive day of the campaign was the 7th of July, when a map of tropospheric NO_2 VCDs was retrieved with the APEX imaging spectrometer. On the same day, NO_2 NSCs and VCDs were measured with two vehicles from the Ludwig Maximilian University of Munich (LMU) and the Max Planck Institute for Chemistry (MPIC). Both vehicles were equipped with NO_2 in situ monitors and mobile MAX-DOAS instruments for measuring NSCs and VCDs, respectively. In addition, stationary measurements were conducted at LMU's Meteorological Institute Munich (MIM) near the city center, at the Oscar-von-Miller (OvM) northeast of Munich, and near the combined heat and power (CHP) plant Munich South. In the following, the different measurements are described in more detail.

2.1 Meteorological observations

Meteorological parameters were measured every minute at the MIM and the OvM tower at different altitudes. Air temperature, air pressure, wind speed and direction, and global radiation are available. Wind speeds and directions were measured on the MIM's rooftop at 30 m above ground. At the OvM tower, temperature and wind speeds were measured at 2, 5, 10, 20, 35 and 50 m above ground as well as wind directions at 10 and 50 m. Wind information is also available from measurements at the Munich South CHP plant site at 15 m above ground and from the COSMO-1 and COSMO-7 model analysis product of the Swiss Federal Office of Meteorology and Climatology (MeteoSwiss).

2.2 Monitoring stations

The Bavarian Landesamt für Umwelt (LfU) is operating a network of five monitoring stations in Munich (Fig. 1) measuring hourly concentrations of several air pollutants including NO_2 and meteorological parameters. The network consists of two
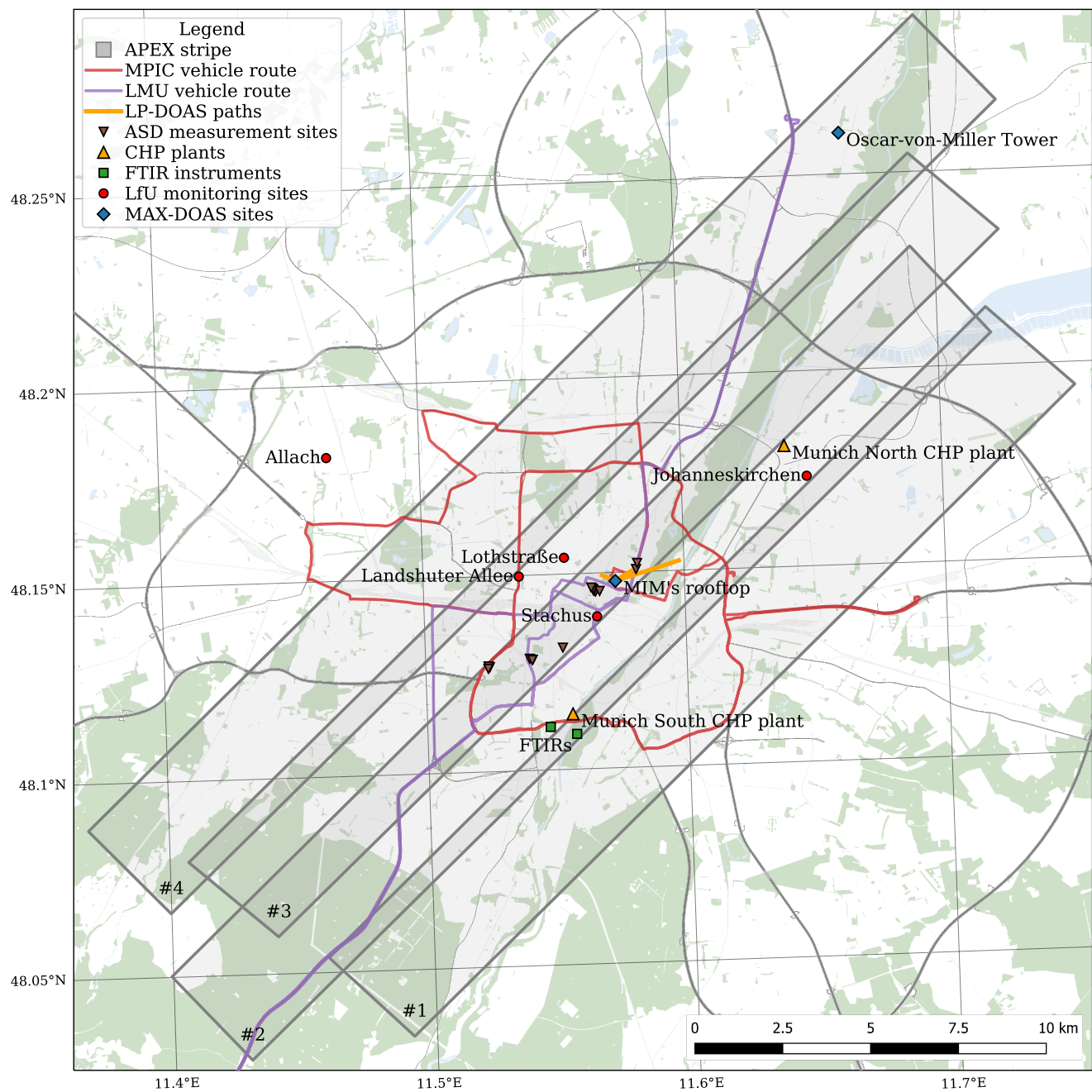
Figure 1. Map of Munich with overlayed APEX flight stripes (#1-4), routes taken by the LMU and MPIC vehicles in the afternoon of 7 July 2016 as well as locations of combined heat and power (CHP) plants, FTIR instruments, LfU monitoring sites, stationary MAX-DOAS instruments and the locations of surface reflectance measurements with the ASD instruments. Map data from © OpenStreetMap contributors 2021. Distributed under the Open Data Commons Open Database License (ODbL) v1.0.

Table 1. Instruments and their measurements available during MuNIC on 7 July 2016.

Instrument	Operators	Parameters	Measurement location	Measurement times (UTC)
APEX	Empa, UZH	trop. NO_2 VCDs, HCRF	DLR aircraft	12:16 - 12:56
Mini MAX-DOAS	MPIC	trop. NO_2 VCDs	LMU vehicle	7:50 - 9:55, 11:30 - 15:30
Tube MAX-DOAS	MPIC	trop. NO_2 VCDs	MPIC vehicle	8:00 - 9:45, 11:15 - 15:30
CE-DOAS	LMU	NO_2 NSCs	MPIC vehicle	8:10 - 9:40, 11:30 - 15:30
CAPS	Empa	NO_2 NSCs	LMU vehicle	7:50 - 9:55, 11:15 - 15:30
MAX-DOAS (OvM)	LMU, USTC	NO_2 profiles	OvM tower	none
MAX-DOAS (MIM)	LMU	NO_2 profiles	MIM roof	6:56 - 16:10
LP-DOAS	LMU	NO_2 NSCs	MIM roof	all day
Bruker EM27/SUN FTIRs	TUM	XCO_2, XCH_4	Munich South CHP plant	9:20 - 16:10
ASD	Empa, LMU, UZH	HCRF	hand held	9:00 - 14:30

suburban background stations (Allach and Johanneskirchen), one urban background station (Lothstraße), and two urban road-side stations at (Landshuter Allee and Stachus). NO_2 is measured with standard chemiluminescence NO_x analyzers, which use heated Molybdenum catalysts to convert NO_2 to NO before detection.

2.3 LP-DOAS

A long-path DOAS system was installed at the MIM's rooftop at 25 m above ground. The system measures the mean NO_2 concentrations along optical paths between the instrument and retro-reflectors installed at neighboring buildings using a blue light-emitting diode (LED). The sampling time ranges from 30 to 90 s depending on visibility conditions. The measurement setup and the NO_2 retrieval is described in detail by Zhu et al. (2020). Three optical paths were operated during the campaign (Fig. S1 in the supplement): a 816 m path to the rooftop of the N5 building of the Technical University of Munich (TUM) with the retro-reflector installed at 28 m above ground, a 2174 m path to the rooftop of the LMU physics building at 28 m above ground, and a 3828 m path to the rooftop of the Hilton hotel building at 48 m height. The light paths cover the university campus, a public park, residential areas and several roads.

2.4 Stationary MAX-DOAS

NO_2 profiles above roof level were measured with a MAX-DOAS instrument at the MIM's rooftop in the city center and a second MAX-DOAS instrument on top of the OvM tower about 15 km northeast to the city center. Unfortunately, no measurements are available at the OvM tower for 7 July 2016 due to technical issues of the instrument.

The MAX-DOAS was programmed to measure scattered solar radiances at 9 elevation angles (2, 3, 4, 5, 6, 8, 15, 30 and 90°) and 7 azimuth angles (0, 90, 135, 180, 225, 270 and 315°). In this study, only measurements at an azimuth angle of 0°(pointing northwards) were analysed from which differential NO_2 slant columns (dSCDs) were retrieved using a DOAS analysis for a

wavelength range from 425 to 490 nm. The DOAS analysis considered NO_2, O_4, O_3 and H_2O absorption cross sections, a Ring spectrum as well as a polynomial of degree 5. Small shift and squeeze of the wavelength are allowed in the wavelength mapping process to compensate for small uncertainties caused by the instability of the spectrograph.

Aerosol extinction coefficient profiles were retrieved from the O_4 absorption bands at 477 nm using the Munich Multiple wavelength MAX-DOAS retrieval algorithm (M^3), described in detail in Chan et al. (2018, 2019, 2020). Due to the systematic discrepancy between observation and model simulation of O_4 DSCDs (e.g., Wagner et al., 2009), all MAX-DOAS observations of O_4 DSCDs are multiplied with a correction factor of 0.8 (see Chan et al., 2019, for details). The algorithm uses the optimal estimation method (Rodgers, 2000) and the libRadtran radiative transfer code as the forward model (Mayer and Kylling, 2005; Emde et al., 2016). The aerosol profiles obtained from the procedure are used for the calculation of air mass factors for discrete vertical layers (1D-layer AMF) required for NO_2 profile inversion. The layer AMFs are calculated at 477 nm for the retrieval of NO_2 profiles using the Monte Carlo solver (MYSTIC) of libRadtran (Emde et al., 2016; Schwaerzel et al., 2020).

2.5 Airborne Prism Experiment (APEX)

APEX is a push-broom imaging spectrometer that has been developed for environmental monitoring (Schaepman et al., 2015). It measures radiance spectra with an optimized integration time simultaneously in 1000 across-track spatial pixels within a $28°$ field of view. At a flight altitude of 7360 m above ground, its spatial resolution is about $4\,\text{m} \times 6\,\text{m}$ in across- and along-track direction, respectively. The along-track resolution is computed from aircraft altitude, ground speed and integration time. For each pixel, spectral radiance is measured in the visible and near-infrared (VNIR, 372 - 1015 nm) and shortwave infrared (SWIR, 940 - 2540 nm) channel. To retrieve NO_2 VCDs, spectra were acquired in the unbinned mode providing the highest nominal spectral resolution of 0.86 nm full-width-at-half-maximum (FWHM) and 0.45 nm spectral sampling interval (SSI) in the VNIR channel with 334 spectral bands. Note that FWHM and SSI vary with wavelength and range from 0.86 to 15 nm (FWHM) and 0.45 to 7.5 nm (SSI), owing to the dispersion characteristics of the VNIR prism.

The APEX measurements were acquired along four pre-defined stripes shown in Fig. 1 on 7 July 2016 in the early afternoon (14:16 - 14:56 CEST). The four stripes cover a large fraction of the city with a large overlap between the stripes to increase the amount of APEX observations in the city center where most ground-based observations were conducted. In addition, the stripes cover forest and agriculture land that were used as background spectra in the DOAS retrieval.

APEX NO_2 retrieval algorithms were developed at Empa in Switzerland (Popp et al., 2012) and at BIRA in Belgium (Tack et al., 2017) using the QDOAS software for the DOAS analysis and the LIDORT radiative transfer model for AMF computations. In this study, we used a new version of the Empa APEX NO_2 retrieval algorithm, which has been completely rewritten using Python allowing for automatic and parallel processing of APEX measurements. The new version uses the Python library flexDOAS for the DOAS analysis (Kuhlmann, 2021b) and the Monte Carlo MYSTIC solver for AMFs (Schwaerzel et al., 2020).

To increase the signal-to-noise ratio for the NO_2 retrieval, 20×10 APEX pixels were spatially binned in across- and along-track direction, respectively. As a result, the spatial resolution of the APEX instrument is reduced to about $80\,\text{m} \times 60\,\text{m}$. An in-flight spectral calibration was conducted to improve the accuracy of center wavelength positions and the full-width-at-half-

maximum (FWHM) of the instrument's slit function (Kuhlmann et al., 2016). This was required because the default spectral calibration provided by the APEX processing and archiving facility (Hueni et al., 2009, 2013) was not sufficiently accurate for the retrieval of NO_2.

NO_2 dSCDs were retrieved from the spatially binned APEX spectra using flexDOAS. The last 50 spectra at the western end of each stripe were used as reference spectrum for each across-track position. The DOAS analysis was applied to a window from 470 to 510 nm where we fitted NO_2 and O_4 absorption cross sections, a Ring spectrum, a 5-degree polynomial as well as a relative offset fitted as a quadratic polynomial that was subtracted both from the measurement and reference spectrum. The cross sections of O_3 and H_2O are not considered due to cross correlations and overparameterization in the small fitting window (Popp et al., 2012; Tack et al., 2017).

The NO_2 dSCDs are the differences between SCDs in the observation and reference spectra:

$$dSCD = SCD - SCD_{ref} \tag{1}$$

which are solved for tropospheric VCDs using $SCD = AMF \cdot VCD$ as

$$VCD = \frac{dSCD + VCD_{ref} \cdot AMF_{ref}}{AMF} \tag{2}$$

where VCD_{ref} and AMF_{ref} are the reference VCDs and AMFs for each across-track position. Mobile MAX-DOAS observations conducted in the reference area during the APEX flight were used as reference VCDs (VCD_{ref}).

To calculate the AMFs, 1D-layer AMFs were computed with the MYSTIC solver of the libRadtran model (Emde et al., 2016; Schwaerzel et al., 2020) depending on sun position, instrument viewing direction, surface reflectance, surface elevation and atmospheric scattering by molecules and aerosols using an US standard atmosphere. Surface reflectances were taken from the APEX surface reflectance product at 490 nm (c.f. Sec. 2.8) in the center of the DOAS fitting window assuming Lambertian equivalent reflectance (LER). Aerosol scattering was included using an aerosol optical depth of 0.10 measured by the AERONET station at the MIM's rooftop and libRadtran's default aerosol profile. Total AMFs were computed from the 1D-layer AMFs using the NO_2 profile measured by the MAX-DOAS instrument at the MIM's rooftop.

The APEX NO_2 VCDs were destriped to account for small variations of dSCDs and true VCD_{ref} in across-track direction by subtracting deviations from a cubic polynomial fitted to the mean across-track VCDs. In addition, we performed a bias-correction between the different aircraft overpasses by adding a constant offset to each stripe so that the mean values of the overlapping parts of two neighbouring stripes are identical. Both the across-track variations as well as the difference between stripes are mainly caused by differences in spectral and radiometric calibration (Kuhlmann et al., 2016). The NO_2 VCDs were then mapped on a longitude-latitude grid with about 10 m resolution for comparison with the ground-based observations using the gridding algorithm of Kuhlmann et al. (2014) (Code repository: Kuhlmann, 2021c).

The uncertainties in NO_2 VCDs were calculated as the quadratic sum of the uncertainties in dSCDs, AMFs, and SCD_{ref}:

$$\sigma_{VCD} = \sqrt{\left(\frac{\sigma_{dSCD}}{AMF}\right)^2 + \left(\frac{\sigma_{SCD_{ref}}}{AMF}\right)^2 + \sigma_{AMF}^2 \left(\frac{VCD}{AMF}\right)^2} \tag{3}$$

where σ_{dSCD} was estimated from the DOAS analysis. The uncertainties in AMFs and SCD_{ref} were estimated from the comparison with the ground-based remote sensing observations conducted during the campaign.

2.6 Mobile measurements

Mobile measurements were conducted with two vehicles operated by MPIC and LMU, respectively. Each vehicle was equipped with an in situ instrument measuring near-surface concentrations (CE-DOAS and CAPS) and a spectrometer measuring NO_2 column densities (Tube and Mini MAX-DOAS) (see Table1). The measurements were conducted along varying routes in the city. The MPIC vehicle mostly drove circles in the city center to capture the NO_2 fields in across-track direction of the APEX measurements, while the LMU vehicle was driving from the southwest to the northeast of the city along the highway or on smaller roads in the city center to sample in the along-track direction of APEX.

2.6.1 Mobile in situ instruments

Near-surface NO_2 concentrations were measured with two highly sensitive and specific in situ instruments: A T500U CAPS NO_2 Analyzer from Teledyne API that is routinely used in the Swiss National Air Pollution Monitoring Network (NABEL). CAPS consists of a blue LED, a measurement chamber with two highly reflective mirrors and a vacuum photodiode detector. The instrument uses the Cavity Attenuated Phase Shift (CAPS) technique to directly measure NO_2 (Kebabian et al., 2005, 2008). The CAPS was installed in the LMU vehicle with the sample inlet fixed at the roof of the vehicle at about 2 m height. The NO_2 concentrations were recorded every 2 s.

The second instrument was the Broadband Cavity Enhanced Differential Optical Absorption Spectroscopy (CE-DOAS), which uses a blue LED, a measurement chamber and a spectrometer to obtain NO_2 concentrations using the DOAS technique between 435.6 and 455.1 nm (Platt et al., 2009; Zhu et al., 2020). The CE-DOAS was installed in the MPIC vehicle with the inlet located at the front right window of the vehicle at 1.5 m above the ground and measurements were recorded every 2 s.

CAPS and CE-DOAS agreed well when operated together on the LMU vehicle on 1 and 4 July 2016. Pearson correlation coefficients were 0.995 and 0.984 and root mean square errors (RMSE) were 6.1 and 5.9 ppbv on the two days. The difference between CAPS and CE-DOAS are due to instrument differences such as length of tubing and integration times, the short measurement interval of 2 seconds, and the high variability of NO_2 concentrations on roads. Furthermore, it was necessary to shift CAPS measurements by 16.9 s and 5.6 s, respectively (Fig. S2). The time differences were caused by non-synchronised computer clocks and the differences in tubing and integration times. On campaign day, GPS times were used to minimize time differences between instruments.

2.6.2 Mobile MAX-DOAS measurements

The mobile MAX-DOAS measurements were carried out using two instruments operated by MPIC: The Tube MAX-DOAS, which was mounted on the MPIC vehicle, is a scientific grade instrument with a high signal-to-noise ratio and stable spectroscopic properties (see e.g., Kreher et al., 2020). The Mini MAX-DOAS is a more compact instrument but with lower signal-to-noise ratio and less stable spectral properties (see e.g., Shaiganfar et al., 2011). This instrument was mounted on the LMU vehicle. Because of the different signal-to-noise ratios, the total integration times for individual measurements were set to 30 s for the Tube MAX-DOAS and 60 s for the Mini-MAX-DOAS instruments, respectively. The obtained spectra are

averages of multiple single measurements with integration times adjusted according to current sky conditions. Mean individual integration times were roughly 65 ms leading to number of scans of roughly 460 and 920 for the two instruments, respectively. One complete elevation sequence contained 6 (Tube MAX-DOAS) or 7 (Mini MAX-DOAS) measurements at low (22°) elevation angle, followed by one measurement in zenith direction. The line of sight of the Mini MAX-DOAS instrument was in driving direction and the one of the Tube MAX-DOAS instrument was directed backwards with respect to the driving direction. NO_2 was analysed in the spectral range from 400 to 439 nm using a fixed daily Fraunhofer reference measured in zenith direction. Only results with root mean square (RMS) values below 8×10^{-4} (Tube MAX-DOAS) and below 2×10^{-3} (Mini MAX-DOAS) were considered for further processing. The method described in Wagner et al. (2010) and Ibrahim et al. (2010) was applied to determine the NO_2 absorption in the Fraunhofer reference spectrum and to correct for the changing stratospheric NO_2 absorption.

2.7 Fourier transform infrared (FTIR) spectrometers

Two ground-based Fourier transform infrared (FTIR) spectrometers were deployed near the Munich South CHP plant to measure column-averaged dry air mole fractions of CO_2 and CH_4 (XCO_2 and XCH_4). The instruments are owned by Karlsruhe Institute of Technology (KIT) and Technical University of Munich (TUM) and are identified as EM27 KIT and EM27 TUM, respectively. Both instruments are operated by TUM.

The compact and mobile solar-tracking FTIR spectrometers (Bruker EM27/SUN, Gisi et al. (2012)) point towards the sun during measurements and measure spectra in the wavenumber range from 6000 to 9000 cm^{-1}. By placing one spectrometer upwind and the other downwind of the CHP plant, differential column measurements (DCM) can be used to determine the CO_2 and CH_4 emissions from this source. DCM have proven to be an effective method for determining emissions from different types of sources (Hase et al., 2015; Chen et al., 2016; Dietrich et al., 2021; Toja-Silva et al., 2017; Zhao et al., 2019). Differential column measurements exhibit a very high precision of 0.01% for XCO_2 and XCH_4 at 10-min. integration time (Chen et al., 2016; Hedelius et al., 2016).

To capture the emission plume, the spectrometers were placed based on the forecasted wind direction. On 7 July 2016, the wind was blowing from the northwest in the morning turning to northeast in the afternoon. One spectrometer was placed southwest of the CHP plant to capture the plume in the morning and the other spectrometer south to capture the plume at noon. As a result, the stations acted alternately as downwind sites and as background sites throughout the day.

2.8 Surface reflectance

Surface reflectance is a critical input parameter for the AMF computation, because uncertainties in the reflectance can have a strong impact on the NO_2 VCDs. The APEX reflectance product calculates hemispheric-conical reflectance factors (HCRF; Schaepman-Strub et al., 2006) using the atmospheric correction software ATCOR-4 (Richter and Schläpfer, 2002). In short, atmospheric water vapour and aerosol optical depth are estimated from APEX radiance data, which are used, together with other parameters describing the sun-observer geometry, to obtain representative atmospheric transfer functions (e.g. transmittance, spherical albedo, path radiance). The transfer functions were pre-calculated with MODTRAN-5 (Berk et al., 2005) and stored

in a look-up table. Radiance data are also used to estimate spectral-non-uniformities (e.g., spectral shift, band broadening). This information is essential to spectrally convolve identified atmospheric transfer functions and eventually retrieve HCRFs.

To evaluate the APEX surface reflectance product, HCRF spectra were collected with a hand-held Analytical Spectral Device (ASD) field spectroradiometer during the campaign. In total, 14 spectra were measured on 7 July 2016 from 11:05 to 16:19 CEST. All ASD measurements were located in the second and third APEX stripe and included surfaces of varying type and brightness. The locations are shown in Fig. 1 and details are listed in Table S1 in the supplement.

3 Results

3.1 Campaign day with APEX overpass

The APEX flight window was part of a larger measurement campaign in June and July 2016 with various targets. The choice of a suitable day for Munich is based mainly on flight permission and weather conditions. The first two weeks of July 2016 were mostly cloudy with daily mean temperatures and wind speeds ranging from 12–27 °C and 1.0–3.9 m s^{-1}, respectively. A favorable situation with almost no clouds was predicted for 7 July 2016 for the area of Munich, which allowed to conduct the APEX measurements in the early afternoon (14:16 - 14:56 CEST).

Figure 2 shows the time series of meteorological parameters (temperature, wind speed and direction and global radiation) measured at MIM and at the OvM tower on this day. In the morning, small cumulus clouds were still present over Munich, which can be seen as a reduction in global radiation. In the afternoon, the clouds mostly vanished making it possible to conduct the APEX flight. Figure S3 shows the true color composite of the APEX measurements showing only a small cloud at the edges of the image.

Wind speeds were low during night (about 1 m s^{-1}) and slightly higher and highly variable during the day (1 to 6 m s^{-1}). The wind directions were mostly northwesterly during day turning to northeasterly in the evening. We estimated the dispersion category during daytime as very unstable (category V) based on the procedure published by the Association of German Engineers, which determines dispersion categories based on tabulated values for wind speed, cloud fraction and hour of day (VDI - Fachbereich Umweltmeteorologie, 2009, Annex A). Wind speed and direction are consistent with the simulations from the COSMO-1 and COSMO-7 analysis products provided by the Swiss Federal Office of Meteorology and Climatology (MeteoSwiss) with 1 km and 7 km spatial resolution, respectively (Fig. S11). The COSMO-1 model with about 1 km resolution shows small convective cells with highly variable 10-m wind speeds over Munich with a similar spatial variability as the temporal variability of the ground measurements.

Figure 3a shows the time series of NO$_2$ NSCs at the monitoring stations on 7 July 2016. The NO$_2$ measurements show a morning peak during rush hour and an increase in the evening when the boundary layer becomes stable again, solar radiation is missing and the sources (traffic) are still active. The APEX flight was performed around the time of lowest NSCs. Concentrations were about 5 ppbv at the two suburban background stations (Allach and Johanneskirchen) and somewhat higher with 11 ppbv at the urban background station (Lothstrasse). Different from these stations, the two urban traffic stations showed only little variations during the day due to their proximity to emission sources. Concentrations during the APEX flight were 35 and
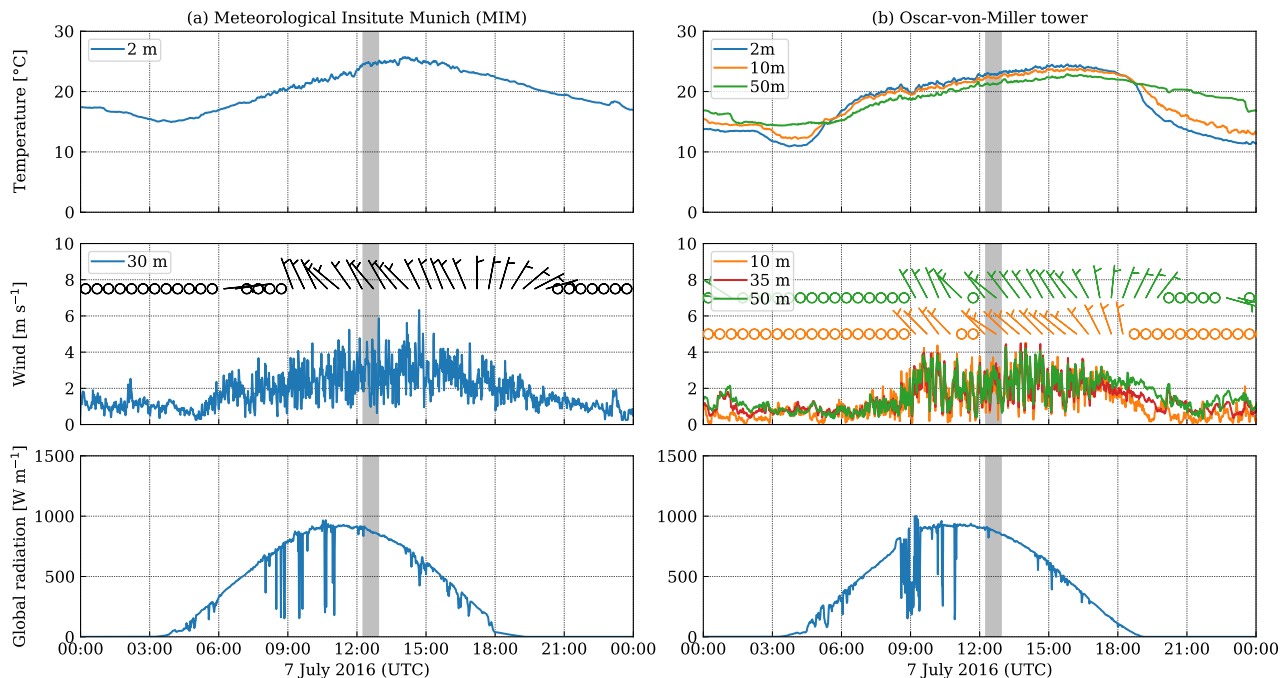
Figure 2. Time series of meteorological observations (temperature, wind speed and direction and global radiation) at (a) Meteorological Institute Munich (MIM) and (b) at the Oscar-von-Miller (OvM) tower. The APEX flight time is shown as gray area.

66 ppbv at Stachus and Lanshuter Allee, respectively. The LP-DOAS also measured the diurnal cycle with molar fractions similar to the suburban background stations due to the elevated light paths measuring NO_2 above the urban canopy. The LP-DOAS measured NO_2 concentrations of about 5 ppbv during the APEX overpass.

The MAX-DOAS instrument on the rooftop (Fig. 3c) measured highest NO_2 VCDs in the early morning with up to 270   504 $\mu mol\,m^{-2}$. NO_2 VCDs dropped substantially to about $104\pm15\,\mu mol\,m^{-2}$ in the afternoon. Note that $100\,\mu mol\,m^{-2}$ are about $6\times10^{15}\,molecules\,cm^{-2}$. Since the temporal variability of NO_2 VCDs was small in the afternoon, differences between mobile and APEX measurements due to different measurement times are likely small.

Figure 3d shows averaged NO_2 profiles retrieved in the morning and in the afternoon. The profiles were retrieved for an azimuth angle of 0 degrees, i.e. looking northwards. The mole fractions in the lowest layer (0 - 200 m) were only 4.6 and 275   2.0 ppbv in the morning and afternoon, respectively, which is smaller than the 8.4 and 3.8 ppbv measured by the LP-DOAS system on average. The averaging kernels of MAX-DOAS retrieval for the lowest layer range between 0.85 and 1, indicating the retrieval reconstruct the lowest layer quite well. However, the lowest layer of the MAX-DOAS represents the average of the lowest 200 m, while LP-DOAS measures at about 30 m above ground. Therefore, it is expected the LP-DOAS measures higher concentration than the MAX-DOAS.
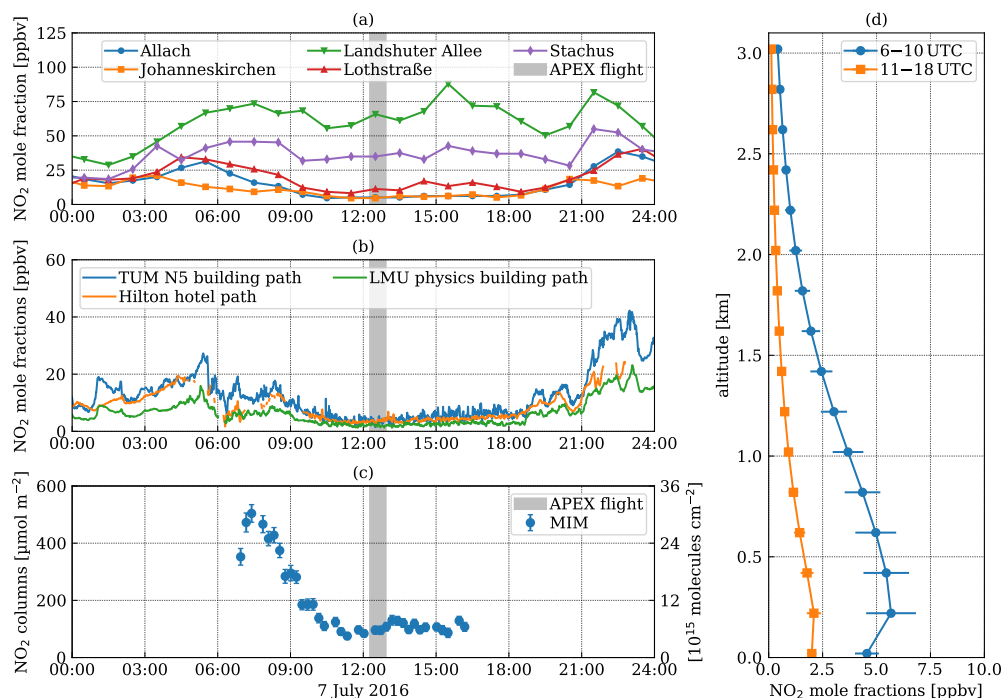
Figure 3. (Time series of NO_2 mole fractions from (a) monitoring stations and (b) the LP-DOAS systems. (c) Time series of vertical column densities and (d) mean NO_2 profiles from the MAX-DOAS instrument on the MIM's rooftop on 7 July 2016.

3.2 Mobile in situ measurements

Figure 4a shows the NO_2 mole fractions along the routes taken by the LMU and MPIC vehicles on 7 July 2016 in the afternoon. The markers for the LfU sites and lines for LP-DOAS show mean values in the afternoon (11:00 - 17:00 UTC). Figure 4b and c show the corresponding time series of NO_2 mole fractions. A corresponding figure showing measurements during the morning (7:00 - 10:00 UTC) is available in the supplement (Fig. S4).

NO_2 mole fractions varied strongly along the route, because they are very sensitive to local emissions. The values ranged from 0 to 890 ppb with highest values being observed in congested areas, in front of traffic light or in tunnels. While 2-second values show high variability along the road, 30-minute averages are similar to hourly measurements at the roadside stations at Stachus and Landshuter Allee when the vehicle passed at distances of 75 m and <10 m from the stations, respectively (Fig. 4b and c). A more detailed comparison of mobile measurements and measuring stations for these data can be found in Zhu et al. (2020).
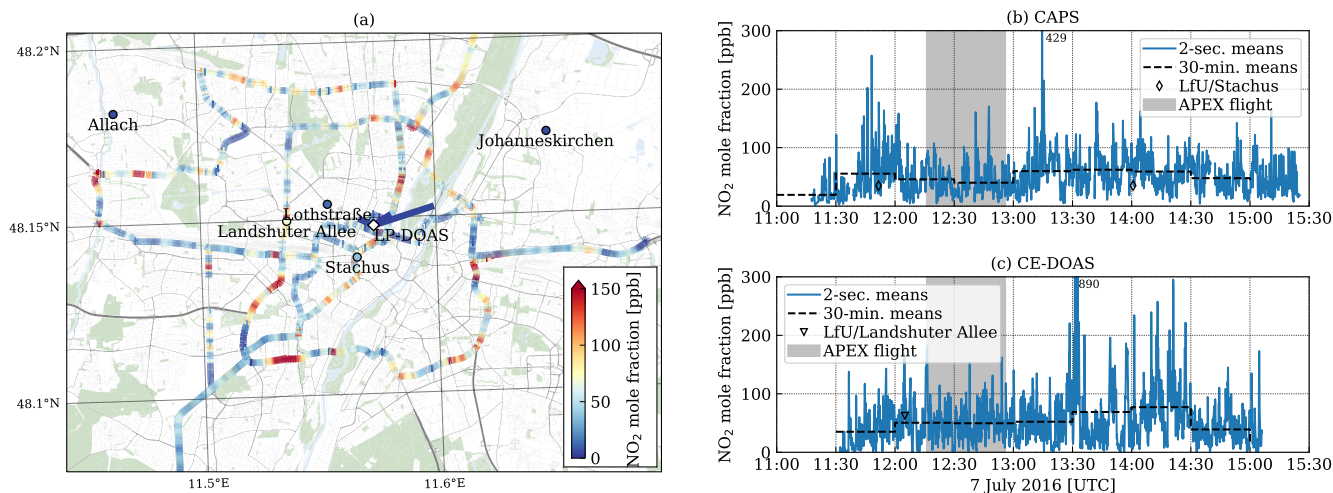
Figure 4. (a) Map of NO_2 mole fractions measured by LMU and MPIC vehicles in the afternoon. Locations of the LfU monitoring stations are shown as circles colored by the mean afternoon NO_2 mole fraction. (b) and (c) show the time series of NO_2 mole fractions measured by the CAPS and CE-DOAS instrument on the LMU and MPIC vehicle, respectively. Map data from © OpenStreetMap contributors 2021. Distributed under the Open Data Commons Open Database License (ODbL) v1.0.

3.3 APEX NO_2 observations

3.3.1 APEX NO_2 retrieval algorithm

The true color images of the four APEX stripes are shown in Fig. S3 in the supplement. The stripes were mostly cloud-free with only a small cumulus cloud in the western edge of the second stripe.

295   The spectral calibration was much more stable than on other flights investigated by Kuhlmann et al. (2016) likely because the measurements were conducted after the long transfer flight from Zurich to Munich prior to the measurements, allowing the system to reach a stable pressure and temperature state. The in-flight spectral calibration shows the known spectral smile of the APEX instrument in across-track direction (Fig. S5a) but no strong drift during data acquisition in along-track direction (Fig. S5b). The instrument slit function is about 30% wider in-flight than the laboratory calibration (see Sec. 2.5), which is

300   a known but not fully understood characteristic of the APEX instrument that is likely related to stray-light and vignetting (Kuhlmann et al., 2016).

    Figure 5 shows an example of the DOAS analysis for an APEX pixel acquired inside the plume of the Munich South CHP plant (stripe: 2, across-track: 42, along-track: 314) with a root mean square (RMS) of 1.22×10^{-3} and an NO_2 dSCD of $621 \pm 130\,\mu\mathrm{mol\,m^{-2}}$.

305   The distributions of RMS, dSCDs, HCRFs, AMFs and VCDs are shown in Fig. 6 for the second stripe. The distributions for the other APEX stripes are shown in the supplement (Fig. S6-S8).
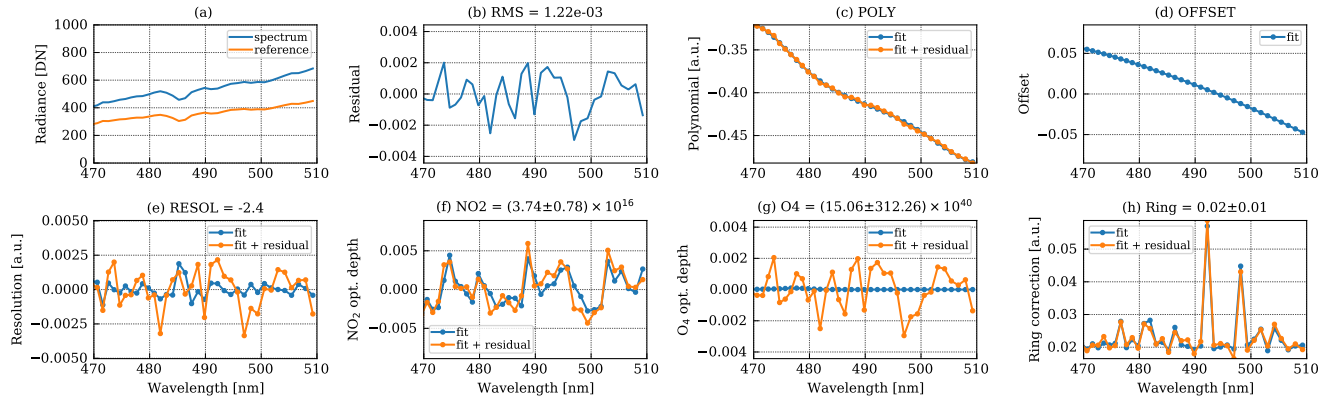
Figure 5. Example for DOAS retrieval for APEX Stripe #2 inside the NO_2 plume of the Heizkraftwerk Süd power plant at across and along-track positions of 42 and 314, respectively: (a) APEX measurement spectrum and reference spectrum, (b) residual, (c) fitted polynomial, (d) fitted offset, (e) resolution cross section, (f) NO_2 optical depth, (g) O_4 optical depth and (h) Ring pseudo cross section.

For all stripes, RMSs do not vary strongly spatially ranging from 0.49 to 1.00×10^{-3} (5th to 95th percentile) with a mean value of 0.73×10^{-3}. The values are smallest in the area used for computing the reference spectra (Fig. 6a). RMS are highest over very bright surfaces and increase with distance from the reference area. This dependency on along-track position is likely caused by a mismatch in spectral calibrations between reference and measurement spectrum that increases with distance from the reference area. RMSs also vary in across-track direction where positions have higher RMS than other also likely caused by small differences in the spectral calibration.

The NO_2 dSCDs show no clear spatial pattern, but values are highest in the middle over the city and lowest at the right side over the forest used as reference area (Fig. 6b). The average dSCDs is $178 \, \mu mol \, m^{-2}$ but values range between -71 and $417 \, \mu mol \, m^{-2}$ (5th to 95th percentile).

HCRFs at 490 nm in the APEX product varied over the city from 0.02 to 0.12 (5th to 95th percentile) with a mean of 0.06. The HCRFs were smaller with an average value of 0.03 (range: 0.01–0.06) over the forest in the west of the city, which was used as a reference area for the DOAS analysis. The AMFs depend mainly on HCRFs and range between 1.1 and 1.9 with an average of 1.5 (Fig. 6d).

The NO_2 VCDs computed from dSCDs and VCDs (Eq. 2) have an average of $115 \, \mu mol \, m^{-2}$ and range from -37 to $294 \, \mu mol \, m^{-2}$ (5th to 95th percentile). The destriping algorithm successfully removes the stripes visible in the dSCDs (Fig. 6e). The destriped VCD field shows clearer features such as two enhancements in the left and centre of the stripe, which match the locations of the Munich North and Munich South CHP plants.
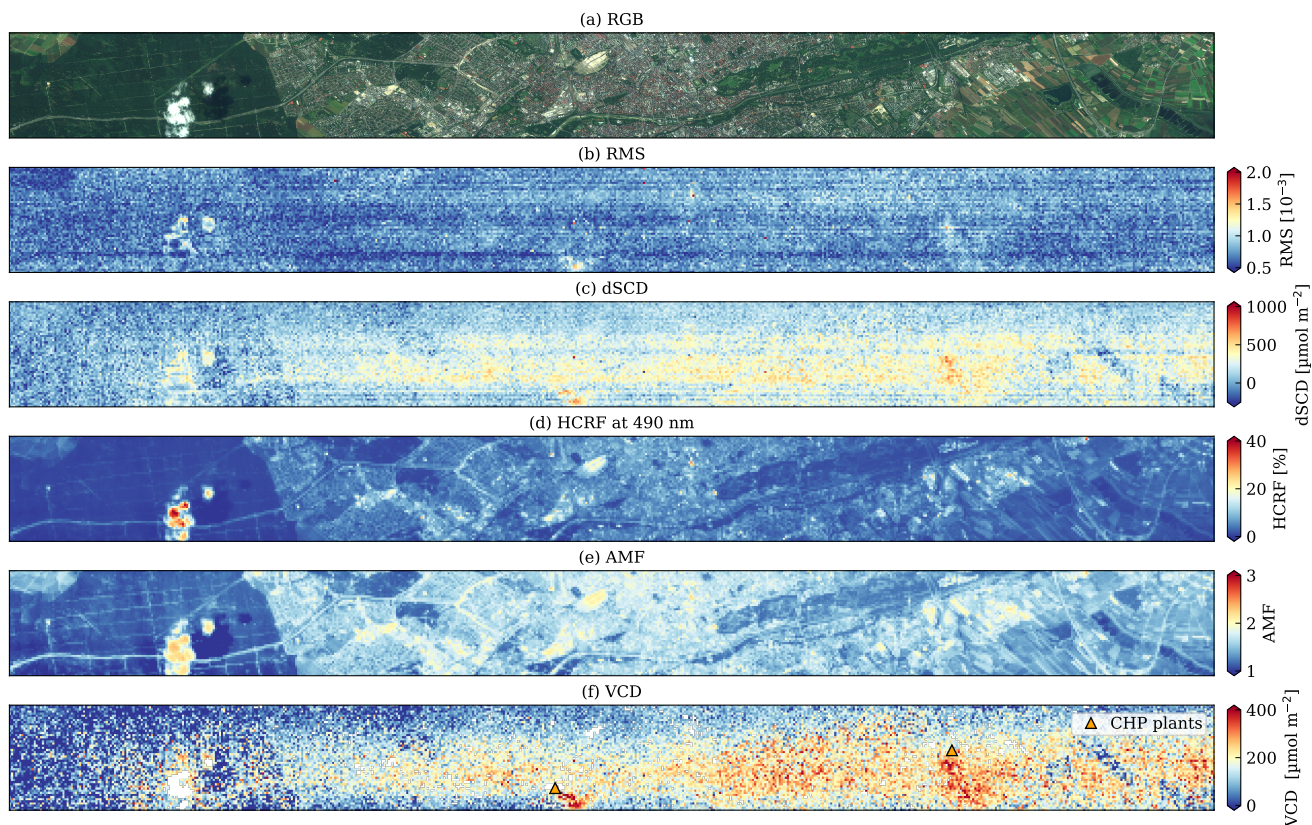
Figure 6. (a) True color image, (b) Root mean square (RMS), (c) NO_2 differential slant column densities (dSCD), (d) hemispheric-conical reflectance factors (HCRF), (e) air mass factors (AMF) and (f) NO_2 vertical column densities (VCD) of the second APEX stripe (see Fig. 1).

3.3.2 APEX NO_2 uncertainties

The uncertainties of the VCDs were obtained from the uncertainties of dSCDs, SCD_{ref} and AMFs (Eq. 3). The dSCD uncertainty was obtained directly from DOAS fitting routine and varied between 18 and 185 $\mu mol\,m^{-2}$ with 56 $\mu mol\,m^{-2}$ on average.

The uncertainties in the AMFs are caused mainly by uncertainties in the surface reflectance product and the a priori NO_2 profile used in AMF calculations. To estimate the uncertainty of the APEX surface reflectance product, we validated the product with the 14 ASD measurements in the city center covered by the second and third APEX stripe (Fig. 1 and S9, and Tab. S1). Figure 7 shows two examples of HCRF spectra over a dark and bright surface. APEX and ASD HCRF agree very well at 490 nm with a correlation coefficient of 0.99, but the APEX product tends to underestimate high reflectances (slope: 1.21, intercept: -0.02). The root mean square difference (RMSD) between APEX and ASD HCRFs is 0.014 considering only ASD values smaller than 0.30, which is a relative uncertainty of about 23% for the mean HCRF over the city (HCRF = 0.06). We
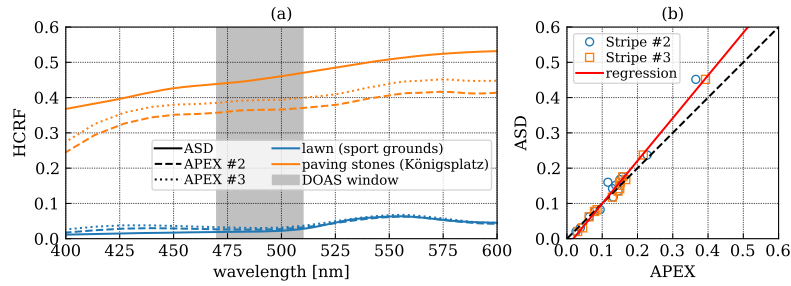
Figure 7. (a) APEX and ASD HCRF spectra for a dark and bright surface. (b) Scatter plot comparing APEX and ASD at 490 nm over all 14 targets. The regression line has a slope of 1.211 and an intercept of -0.022. The correlation coefficient is 0.99.

computed the 1σ uncertainties of the AMFs using an uncertainty of 0.014 in HCRFs, which results in AMF uncertainties of 0.15 and 0.08 for HCRFs of 0.03 and 0.06, respectively.

The uncertainties in the a priori NO_2 profiles translate to about 10% uncertainty in AMFs for satellite NO_2 products (e.g., Boersma et al., 2011). In our study, the a priori NO_2 profile was obtained from the MAX-DOAS instrument on the MIM rooftop, which should provide a representative profile for the city above building level. Since the instrument is not sensitive to near-surface NO_2, we analyzed the impact of the NO_2 profile sensitivity by replacing the mole fraction in the lowest layer (0-200 m) with values ranging from 0 to 100 ppbv. We find that the corresponding AMF uncertainty is smaller than 0.10 for LERs larger than 0.20 and up to 0.16 for a black surface (LER = 0.00).

The total AMF uncertainties are obtained as sum of variances of the individual components (surface reflectance and a priori NO_2 profile). We calculated that AMF uncertainties decrease from 0.40 to 0.10 for LERs increasing from 0.00 to 0.05 and is constant at 0.10 for LERs larger than 0.05. Uncertainties might be somewhat larger, because uncertainties in the aerosol profiles are not taken into account.

The uncertainty of the reference slant column density (SCD_{ref}) was estimated to be about 25% considering the uncertainty of the VCDs retrieved from the Mini MAX-DOAS ($\sigma_{SCD} < 15\%$) and the uncertainty of the AMFs averaged over the forest used as reference area ($\sigma_{AMF} \approx 0.13$).

The VCD uncertainties were computed from Eq. (3). The uncertainty is dominated by the dSCD uncertainty that accounts for 87% of total uncertainty due to the low signal-to-noise ratio of the APEX measurements. The second most important term is the AMF uncertainty accounting for 12% of the total uncertainty while the uncertainty of the reference SCD is small compared to the other two components. Figure 8a shows the estimated uncertainties for the second stripe. The uncertainties are highest over dark surfaces (forest, parks and water surfaces), because the uncertainty inversely depends on AMFs (Eq. 3). The uncertainty ranges from 34 to 86 $\mu mol\,m^{-2}$ (5th-95th percentile) with an average of 56 $\mu mol\,m^{-2}$ (Fig. 8b). Since the uncertainty depends on VCD, uncertainties slightly increase with VCDs (Fig. 8c).
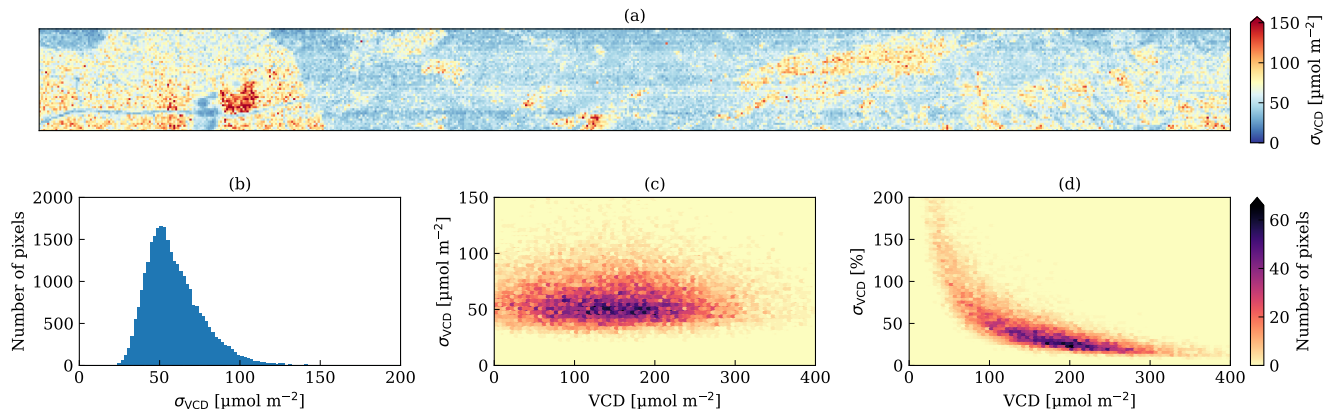
Figure 8. Estimated uncertainty of NO_2 VCDs for the second APEX stripe showing (a) the spatial distribution (see Fig. 1), (b) the distribution of uncertainties and the dependency on the NO_2 VCDs of the (c) absolute and (d) relative uncertainty.

3.3.3 APEX NO_2 map

Figure 9a shows the map of NO_2 VCDs from the APEX instrument. A Gaussian smoothing filter ($\sigma \approx 50$ m) was applied to reduce spatial noise. The map shows lower values in the northwest upwind and higher values in the southeast downwind of the city center. The locations of the Munich North and Munich South CHP plants are marked by two orange triangles. The emission plume of both CHP plants are clearly visible in the APEX data. Otherwise, no small-scale structures, such as roads, can be identified in the map.

While local enhancements related to traffic such as key intersections and highways could be identified in previous APEX campaigns (e.g., Popp et al., 2012; Tack et al., 2017), such structures are missing in Munich likely due to the high variability in wind speed and direction resulting in strong spatial mixing. Recent model studies demonstrate that this is also partially explainable by 3D radiative transfer effects (Schwaerzel et al., 2021).

The APEX NO_2 product also shows artefacts near the stripe edges that are likely related to insufficient knowledge about the spectral calibration and vignetting that affect the accuracy of the instrument slit function (Kuhlmann et al., 2016). The NO_2 map also shows unrealistic low values over water surfaces that also have been noticed by Tack et al. (2017).

3.4 Comparison of APEX and MAX-DOAS observations

Figures 9b and c show the time series of spatially but not temporally collocated APEX and MAX-DOAS NO_2 VCDs, which were obtained by averaging the APEX values along the vehicle paths ± 30 s and ± 15 s for the Mini- and Tube-MAX DOAS, respectively. The LMU vehicle drove along the magenta line (Fig. 9a) leaving the urban area in the southeast and northwest. The time series shows local NO_2 minima when the vehicle was at the southwestern border of the APEX map at 12:20 and 14:35 UTC and at the northwestern border of the APEX map at 13:25 UTC. The MPIC vehicle was driving in anticlockwise
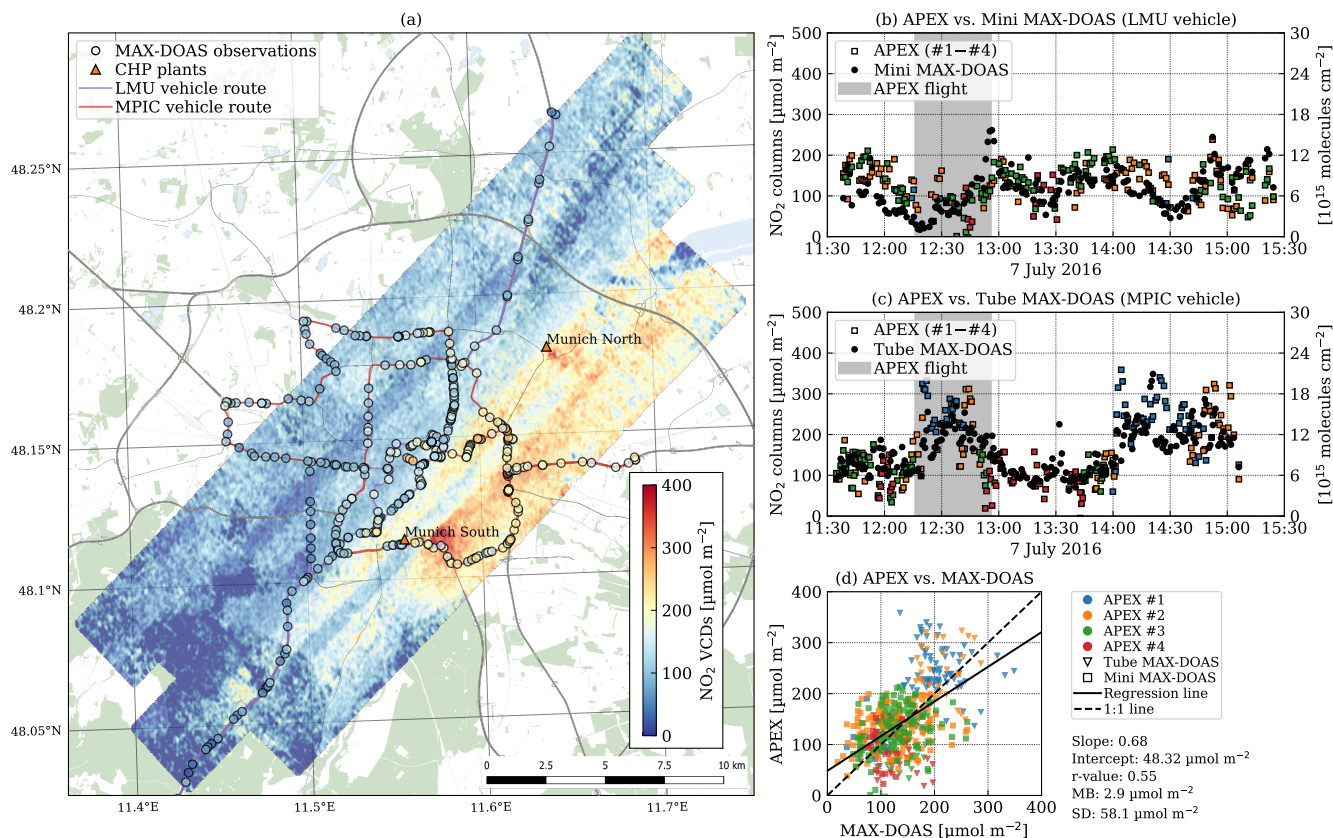
Figure 9. (a) Map NO_2 VCDs from APEX and mobile MAX-DOAS measurements on 7 July 2016 (afternoon). (b,c) Time series of spatially co-located APEX and (b) Mini MAX-DOAS and (c) Tube MAX-DOAS VCDs. (d) Scatter plot showing MAX-DOAS and APEX NO_2 VCDs for spatially co-located observations. Map data from © OpenStreetMap contributors 2021. Distributed under the Open Data Commons Open Database License (ODbL) v1.0.

direction around the city center along the red line in Fig. 9a. NO_2 VCDs were highest when the vehicle was located in the eastern part of the city (12:30 and 14:30 UTC). A map showing the time labels is provided in the supplement (Fig. S10).

In total, 518 co-located APEX and MAX-DOAS observations are available. APEX and MAX-DOAS NO_2 VCDs agree with a moderate correlation coefficient r of 0.55. The regression line has a slope of 0.68 and an intercept of $48.3\,\mu mol\,m^{-2}$.

380 Furthermore, the mean bias (MB) computed from the differences between APEX and MAX-DOAS measurements is close to zero with $2.9\,\mu mol\,m^{-2}$. The standard deviation (SD) of the differences is $58.1\,\mu mol\,m^{-2}$. The discrepancy between airborne and ground-based observations is largely explainable by the relatively high uncertainty of individual APEX and MAX-DOAS NO_2 VCDs (i.e. APEX uncertainties were approximately $60\,\mu mol\,m^{-2}$). In addition, airborne and ground-based instruments do not measure exactly the same air mass due to different viewing directions and different measurement times. Furthermore,

385 the vertical sensitivity to NO_2 is different for APEX and MAX-DOAS, so that inconsistent assumptions about the vertical

profile of NO_2 affects the comparison. It should be noted that APEX and MAX-DOAS observations are not fully independent, because the APEX NO_2 retrieval algorithm uses MAX-DOAS measurements as VCD_{ref}.

3.5 Relationship between near-surface concentrations and vertical column densities

Airborne NO_2 maps from imaging remote sensing instruments can be valuable for studying the spatial distribution of air pollutants in a city. However, to access the impact of NO_2 on human health, it is necessary to transfer VCDs to NSCs using a transfer parameter t such that:

$$NSC = t \cdot VCD. \tag{4}$$

The parameter t (in m^{-1}) is the ratio of NSC (in $\mu mol\,m^{-3}$) and VCD (in $\mu mol\,m^{-2}$). It depends on the shape of the vertical NO_2 profile, which varies in space and time with local NO_x emissions, meteorological factors such as wind speed and vertical mixing, NO_x chemistry and NO_2 advected from the surroundings.

In the MuNIC campaign, both NSCs and VCDs were measured simultaneously by the in situ monitors and the MAX-DOAS instruments aboard the MPIC and LMU vehicle. It is therefore possible to calculate the ratio of NSCs and VCDs and to study the spatial variability of the transfer parameter. Figure 10a shows the spatial distribution of the ratio on 7 July 2016 (afternoon). The ratios are highest outside the city plume where VCDs are low but NO_2 NSCs on the roads are still high. In contrast, ratios are small inside the plume where both NSCs and VCDs are high, but NSCs make up a smaller fraction of the total column. The raios vary strongly along the roads due to the highly variable NO_2 concentrations due to traffic emissions. We did not measure NSCs away from roads, but since NSCs tend to be smaller away from roads and VCDs do not show much spatial variability, we expect lower and less variable values there.

A constant transfer parameter can be obtained by fitting the NSC on the VCD measurements using Eq. (4). Figure 10c shows the scatter plot and the fitted lines. The parameter t is $0.014\,m^{-1}$ when using measurements from both the MPIC and LMU vehicle. The root mean square error (RMSE) is large with $1.5\,\mu mol\,m^{-3}$ or 34.7 ppbv showing that estimated NSCs from airborne observations would be highly uncertain. The estimate can likely be improved when considering additional factors such as local emissions and emissions upstream of a location as NSCs are very sensitive to local emissions, while VCDs from MAX-DOAS and airborne imagers are more representative for larger areas (Irie et al., 2011; Schwaerzel et al., 2020, 2021).

3.6 NO_x and CO_2 emissions of point sources

The two largest point sources in the city are the Munich North CHP plant and Munich South CHP plant (see Fig. 1). For 2016, Munich North reported CO_2 and NO_x mean emissions of $80\,kg\,CO_2\,s^{-1}$ and $53\,g\,NO_2\,s^{-1}$, respectively, and Munich South reported $26\,kg\,CO_2\,s^{-1}$ and $14\,g\,NO_2\,s^{-1}$ (European Environment Agency, 2021). Since instantaneous emissions usually differ from annual means, we calculated the instantaneous emissions of Munich South using the natural gas consumption provided by the operating Stadtwerke München (SWM) using a conversion factor of $1.9225\,kg\,CO_2$ per Nm^3 natural gas (U.S. EPA, 2016) and the mass ratio of annual CO_2 and NO_x emissions. The computed emissions are $44.2\,kg\,CO_2\,s^{-1}$ and
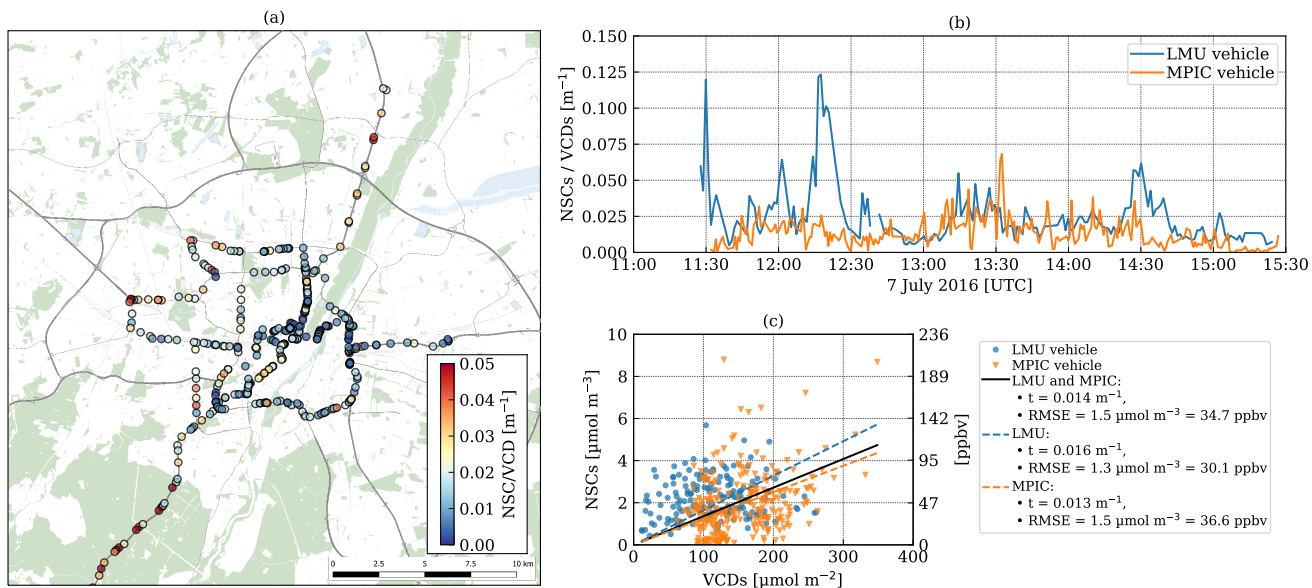
Figure 10. (a) Map of ratios of NO_2 near-surface concentrations (NSC in $\mu mol\,m^{-3}$) to vertical column densities (VCD in $\mu mol\,m^{-2}$) measured by in situ monitors and MAX-DOAS on-board the LMU and MPIC vehicle. (b) The time series of ratios measured with the two vehicles, (c) a scatter plot of NSCs and VCDs. Map data from © OpenStreetMap contributors 2021. Distributed under the Open Data Commons Open Database License (ODbL) v1.0.

23.1 $g\,NO_2\,s^{-1}$, which is about 70% higher than annual means, and only vary slightly by $\pm 1.3\,kg\,CO_2\,s^{-1}$ and $\pm 0.7\,g\,NO_2\,s^{-1}$ between 9:30 and 14:00 UTC on 7 July 2016.

CO_2 and NO_x emissions can be estimated from CO_2 and NO_2 observations. APEX flew once over Munich North at 12:27
420 UTC (Stripe 2) and twice over Munich South at 12:18 and 12:29 UTC (Stripe 1 and 2). The NO_2 emission plumes of the two CHP plants are visible in the APEX observations (Fig. 11a,e and h). In addition, the CO_2 plume of Munich South was observed by the FTIR spectrometers (Fig. 12).

Figure 12a shows the setup of the two FTIR spectrometers where the instruments can observe XCO_2 upwind and downwind of the plume. The XCO_2 time series of the instruments is shown in Fig. 12c. The KIT instrument frequently observed the CO_2
425 enhancement of the CHP plant plume downwind of the source, while the TUM instrument observed the upwind values. Since the plume location meanders depending on wind speed and direction, the line-of-sight of the FTIR instrument will not always include the plume. In fact, during the APEX measurements, the FTIR instruments did not capture any CO_2 enhancements, because the line-of-sight followed the sun towards the west, while the wind carried the plume towards the southeast. Figure 12b shows the APEX NO_2 field overlayed with the line-of-sights of the two FTIR spectrometers confirming that the plume
430 was not in the instrument's field of view at APEX overpass time.
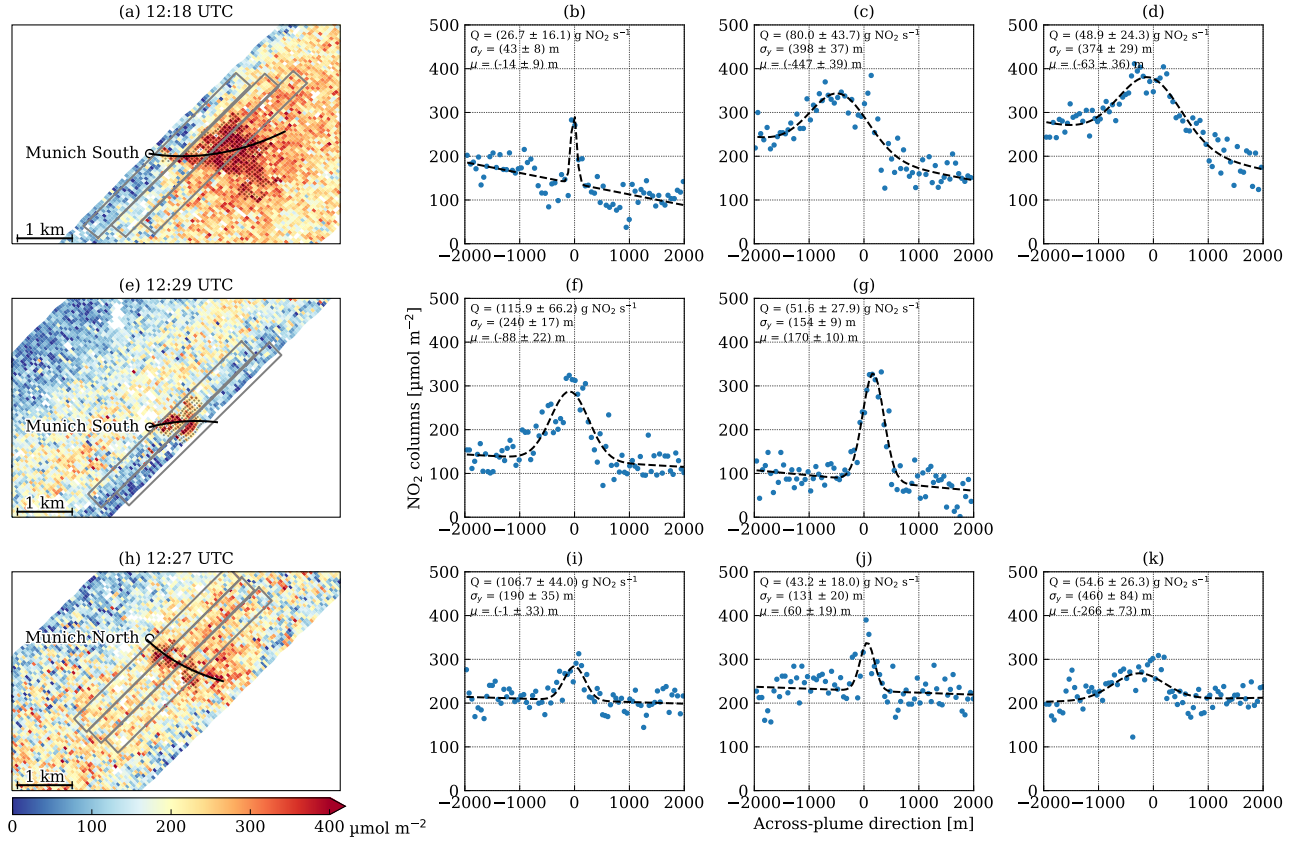
Figure 11. (a,e,h) APEX NO_2 maps with emission plumes (black dots) of the Munich South and Munich North CHP plant. The centerline of the plume is shown as black curve. (b-d,f,g,i-k) APEX NO_2 VCDs averaged in across-track direction within gray boxes shown in the maps and a Gaussian curve fitted to the observations (dashed line).

3.6.1 NO_x emissions

The NO_x emissions of Munich North and Munich South CHP plants were estimated from the APEX observations using a plume detection algorithm and mass-balance approach implemented as part of a Python package for "Data-driven Emission Quantification" (Kuhlmann, 2021a; Kuhlmann et al., 2021). The NO_x emissions Q were obtained by computing the cross-sectional flux as

$$Q = f(x) \cdot q(x) \cdot u(x) \cdot \cos\left(\alpha(x)\right) \tag{5}$$

where x is the along-plume coordinate, f is the NO_2:NO_x conversion factor, q is the line density and $u\cos(\alpha)$ is the wind speed normal to the cross section used for computing the line density. The line density was computed by fitting a Gaussian curve to the along-track NO_2 VCDs:

$$VCD(y) = \frac{q}{\sqrt{2\pi}\sigma} \exp\left(-\frac{(y-\mu)^2}{2\sigma^2}\right) + my + b \tag{6}$$
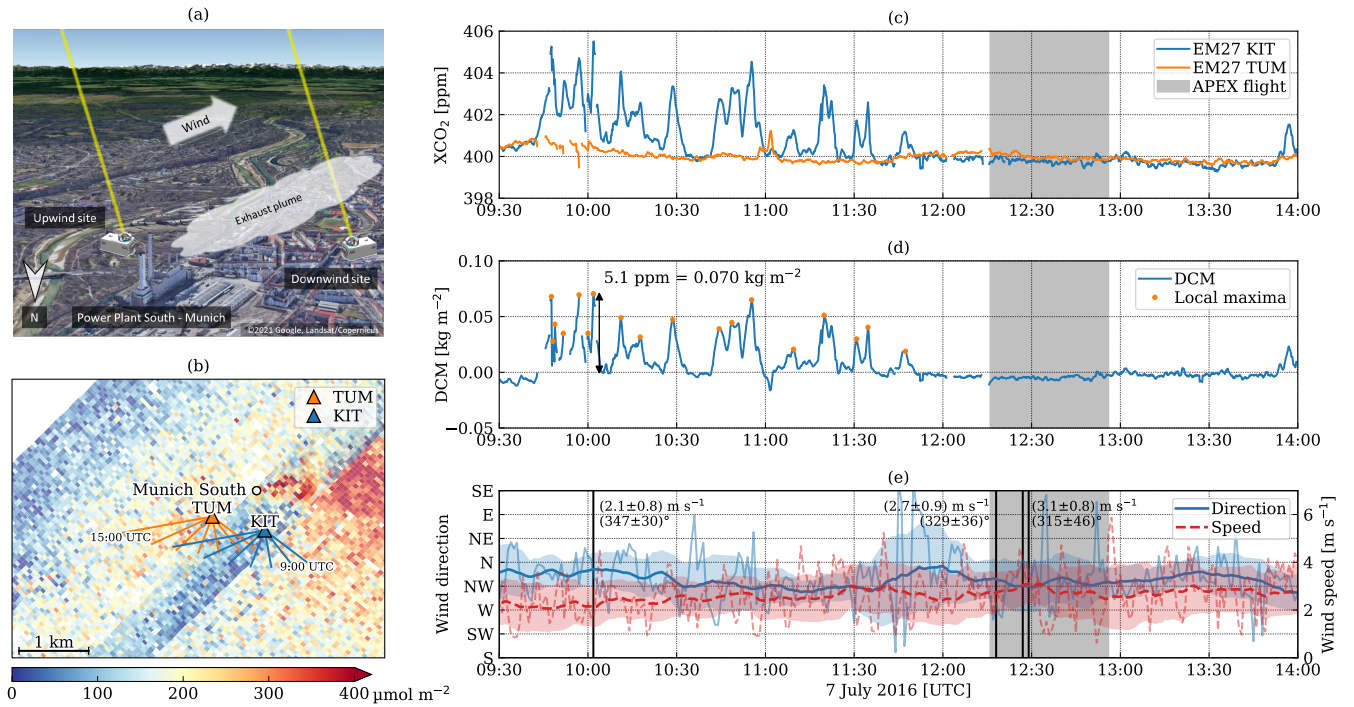
Figure 12. (a) The setup of the two FTIR spectrometers at Munich South. (b) APEX NO_2 map showing the NO_2 emission plume and the location of the FTIR spectrometers. The lines are hourly lines-of-sight below $1100\,m$ above ground. (c) XCO_2 time series and (d) differential CO_2 measurements (DCM) for the two instruments. (e) Wind speed and direction measured every minute at LMU rooftop at $30\,m$ above ground (thin lines). In addition, a 30-minute rolling average was applied to the time series (thick lines). The shaded area shows the 1σ temporal variability within 30 minutes. Vertical lines show times with the largest CO_2 peak and NO_2 measurements by the APEX instrument. The numbers are 30-minute mean wind speed and direction.

where y is the across-plume coordinate, μ is a shift and σ is the standard width. The NO_2 background was approximated by a linear function with slope m and intercept b.

To compute the across- and along-plume coordinates, the location and extent of the NO_2 emission plumes was determined using a plume detection algorithm, which detects pixels where the local mean is significantly enhanced above the background (Kuhlmann et al., 2019, 2021). The local mean was computed using a Gaussian filter with standard width of 0.75 pixels. The background was computed as the median of 100 adjacent pixels in along-track direction to avoid issues with across-track stripes. A two-dimensional curve was then fitted to the detected pixels to describe the centerline of the plume. x and y coordinates were computed as arc length from the source and the distance from the curve, respectively. The tangent of the curve was used to determine the wind direction that is used to computed the angle α.

A critical input for estimating the emissions is the wind speed profile, which determines the height of the plume due to plume rise and the wind speed inside the plume. Figure 12e shows the time series of wind speeds and directions measured at the MIM's rooftop at $30\,m$ above ground. The wind speed measured every minute shows high variability with a standard

deviation of about $0.9\,\mathrm{m\,s^{-1}}$ for 30-minute rolling means. Since MIM's rooftop is more than 3 km away from the stacks, the highly variable wind measurements are not well suited as input for estimating emissions. We therefore used the simulations from the COSMO-1 and COSMO-7 analysis products. The 10-m wind fields and vertical profiles are shown in Figs. S11 and S12. Since the COSMO-1 model with about 1 km resolution shows small convective cells whose location is determined by a stochastic process, we average 6×6 grid cells to obtain an average wind profiles and its uncertainty at the stack locations.

The plume height needs to consider plume rise that can be computed from heat emissions, wind speed at the stack and the dispersion category (VDI - Fachbereich Umweltmeteorologie, 1985). Munich South CHP plant has three stacks ($H = 90\,\mathrm{m}$) for which we use heat emissions of 70 MW obtained from the operator. The dispersion category was already determined as very unstable (category: V) in Section 3.1. The wind speed at the height of the stacks is calculated from the COSMO-1 profiles as $2.5\pm1.3\,\mathrm{m\,s^{-1}}$ at 10 UTC. The plume height starts at the 90-m stack and raises quickly to a maximum height of 845 m at about 1580 m downstream of the stack (Fig. S13). We use the wind speed taken from the COSMO-1 profiles at the height of the plume to estimate NO_x emissions. The distance from the plume is given by the arc length of the centerlines. We assume the same heat emissions and stack height to estimate the plume rise for the Munich North CHP plant.

The NO_2:NO_x conversion factor f was computed using an NO lifetime of 0.3 hours for dispersion category V (VDI - Fachbereich Umweltmeteorologie, 2009, Section 10.2) and a residence time, which was computed using the distance from the source to the cross section and the wind speed.

The uncertainties were computed using the uncertainty of the NO_2 VCDs in the Gaussian curve fit and the uncertainty of the wind speed from the spatial standard deviation in the COSMO-1 model. The uncertainty of the wind speed affects the uncertainty directly in Eq. (5) and indirectly due to its impact on the NO_2:NO_x conversion factor. The uncertainty of the conversion factor is also affected by the uncertainty of the NO lifetime, which difficult to quantify as it requires, for example, detailed simulations of the NO_x chemistry in the turbulent emission plume. For the sake of simplicity, we assume an uncertainty of 50% in this study. Since the uncertainty of wind speed is dominating the total uncertainty, additional factors were not included in the uncertainty calculations.

Figure 11a, e and h show the three APEX observations at Munich North and Munich South with the detected pixels (black dots) and centerlines. Line densities were computed by averaging five lines in across-track direction within $\pm2000\,\mathrm{m}$ from the centerline indicated by the rectangular boxes in the figure. The input parameters and the estimated NO_x emissions are shown in Table S2 in the supplement. For Munich South, estimated NO_x emissions range from 26.7 to $115.9\,\mathrm{g\,NO_2\,s^{-1}}$ with an average of $64.6\pm20.3\,\mathrm{g\,NO_2\,s^{-1}}$, i.e. a relative uncertainty of 31%, where the uncertainty is the standard error of the mean. For Munich North, only three line densities could be computed resulting in emissions ranging from 43.2 to $106.7\,\mathrm{g\,NO_2\,s^{-1}}$ (average: $68.2\pm24.8\,\mathrm{g\,NO_2\,s^{-1}}$).

3.6.2 CO_2 emissions

The CO_2 emission strength can be estimated from the differential column measurements (DCM), i.e. the difference between the up- and downstream observations, which represents the enhancement due to the source (Fig. 12a, Chen et al. (2017)). If we assume that the emission plume can be approximated by a Gaussian plume model and that the local peaks in the DCM time

series occur when the plume center moves over the downwind station (i.e. they correspond to the maxima in the Gaussian), the source strength Q would be given by

$$Q = \sqrt{2\pi}\, u(x)\, \sigma_y(x)\, DCM_{max}(x) \tag{7}$$

where u is the wind speed inside the plume, σ_y is the horizontal width of the plume and DCM_{max} is the CO_2 enhancement in the center of the Gaussian plume. Note that u, σ_y and DCM_{max} depend on the distance from the source x.

Figure 12d shows the time series of DCM measured on 7 July 2016. In total, we identified 18 local maxima using a standard peak finding algorithm of the SciPy library (Virtanen et al., 2020, Version 1.4.1) for estimating CO_2 emissions. The highest DCM was measured at 10:02 UTC with 5.1 ppm, which is converted to a mass column density of $0.070\,\mathrm{kg\,m^{-2}}$.

The wind speed was taken from the COSMO-1 profiles to compute plume rise and the distance of the plume from the stack at the slant line-of-sight of the FTIR instrument (Fig. S13). The KIT EM27 spectrometer was located 582 m downstream of the stack. At 10:02 UTC, the line-of-sight of the instrument and the plume height intersect at a height of 615^{+274}_{-177} m. Consequently, the distance from the source x is at 915^{+485}_{-114} m downstream of the source. The dispersion coefficients were computed based on VDI guidelines, which assumes constant coefficients above 180 m. It is computed by an empirical equation $\sigma_y(x) = F \cdot x^f$ with $F = 0.671$ and $f = 0.903$ for the dispersion category V. Therefore, $\sigma_y(x)$ ranges was computed as 317^{+85}_{-36} m at the intersection. The standard deviations were computed from the spatial variability in COSMO-1 wind speeds.

The CO_2 emissions were then computed by Eq. (7) using a wind speed in the plume center of 2.4±0.7 at 615 m above ground, which results in emissions of $134\pm49\,\mathrm{kg\,CO_2\,s^{-1}}$. The uncertainty was estimated using a DCM uncertainty of 0.1 ppm for 1-minute averages (Chen et al., 2016) as well as the uncertainties of $u(x)$ and $\sigma_y(x)$. The uncertainty budget is dominated by the uncertainty in the wind speed that accounts for 72% to the total uncertainty. The uncertainty of the dispersion coefficient σ_y accounts for 27% of the total uncertainty, which also depends on the uncertainty of the wind speed, while the uncertainty of the DCM measurements in neglectable.

The emissions were computed for all 18 peaks and results are shown in Tab. S3 in the supplement. The estimated CO_2 emissions vary strongly ranging from 38 to $134\,\mathrm{kg\,CO_2\,s^{-1}}$. The mean and standard error of all 18 estimates is $81.2\pm8.6\,\mathrm{kg\,CO_2\,s^{-1}}$.

3.6.3 Comparison with reported emissions

CO_2 and NO_x emissions of the Munich South CHP plant were estimated as $81.2\pm8.6\,\mathrm{kg\,CO_2\,s^{-1}}$ and $64.6\pm20.3\,\mathrm{g\,NO_2\,s^{-1}}$ significantly higher than the emissions of $44.2\pm1.3\,\mathrm{kg\,CO_2\,s^{-1}}$ and $23.1\pm0.7\,\mathrm{g\,NO_2\,s^{-1}}$ computed from fuel consumption. The NO_x-to-CO_2 emission ratios are similar between reported and estimated emissions.

The main reason that the estimated emissions are higher than the reported values is likely due to the unstable and highly turbulent atmospheric boundary layer resulting in low and highly variable wind speeds, which makes applying mass-balance approaches challenging for estimating emissions On the one hand, uncertainties are large, because accurate knowledge of the wind speed is critical as it does not only affect the computation of the flux, but also the calculation of plume rise, dispersion coefficient and NO lifetime. On the other hand, mass balance approaches assume stationary conditions, which is not very accurate, especially in turbulent flow conditions.

520   The method applied to estimating CO_2 emissions from the FTIR measurements assumed that the plume can be approximated by a Gaussian plume model and that the local maxima are the maxima in the vertically integrated Gaussian plume. However, maxima in the time series also occur when the wind speed is below the average. As a result, the assumption of an average wind speed would overestimate the CO_2 emissions. The individual COSMO-1 wind profiles (Fig. S12) show that the lower wind speeds would halve the values, which would also lead to a halving of estimated CO_2 emissions much better consistent with our

525 estimate from fuel consumption. The turbulent flow will also result in puff-like structures in the plume where CO_2 values are locally enhanced or reduced compared to a Gaussian model, which will either over- or underestimate emissions. Furthermore, it is possible that only the edge of plume passes briefly through the line-of-sight, which would result in a local maximum but underestimate the emissions. To limit the impact on our estimate, we have estimated emissions for all local peaks in the time series, yet our estimates are still likely to be too high, as the algorithm for identifying peaks does not account for minor peaks.

530   The computation of the cross-sectional flux for estimating NO_x emissions from the APEX NO_2 observations is also limited by the turbulent flow, because the emission plumes are already very wide just 1 km downstream of the source, which makes it difficult to determine the centerline of the plume and the angle between APEX stripe and wind vector. The wind profiles from the simulations and the measurements are less consistent in the afternoon and the COSMO-1 wind profiles might be overestimated (Fig. S12), which could explain the overestimated NO_x emissions. In addition, the estimation of NO_x emissions

535 is sensitive to the NO_2-to-NO_x conversion factor f, which in turn depends on NO lifetime and wind speed. For turbulent flow, the residence time is likely longer than the value computed from mean wind speed and distance from the source resulting in a smaller conversion factor and consequently lower estimated NO_x emissions. Finally, it should also be noted that NO lifetime given by the VDI guidelines might not be sufficiently accurate for conditions on the campaign day.

4   Conclusions

540 In this paper, we presented results from the MuNIC measurement campaign conducted in July 2016 in Munich. The campaign measured NO_2 near-surface concentrations (NSC) and vertical column densities (VCD) with stationary, mobile and airborne in situ and remote sensing instruments. A central element of the campaign was a measurement flight with the APEX imaging spectrometer mapping the spatial distribution of NO_2 VCDs on 7 July 2016 afternoon.

    Our results confirm that airborne imaging remote sensing is suited for spatial mapping of NO_2 VCDs and the detection of

545 emission plumes from larger point sources and cities. The obtained NO_2 VCDs retrievals have a moderate correlation with mobile MAX-DOAS measurements conducted on the same afternoon (r = 0.55) and estimated uncertainties are similar to previous findings (e.g. Tack et al., 2017). The NO_2 map obtained from the APEX data could depict the coarse-scale NO_2 distribution with lower values upwind and higher values downwind of the city but with no strong signatures of individual sources except for the two power plants.

550   We observed substantial differences between VCDs and NSCs. While APEX NO_2 VCDs are not elevated along roads, NSCs show high spatial and temporal variability along roads with highest values in congested areas and tunnels. One reason for these differences is atmospheric mixing, but also 3D radiative transfer effects were recently found to reduce the effective spatial

resolution of the ground pixels and causing random uncertainties in the presence of buildings as well as an underestimation of NO_2 VCDs due to building shadows (Schwaerzel et al., 2021).

The transfer function t required for converting VCDs to NSCs is important when using imaging remote sensing for air pollution studies. However, a constant transfer parameter, calculated as the ratio of NSC over VCD from the observations, results in a very high RMSE when NSCs would be computed from VCDs. More advanced methods (than a simple constant factor) need to be applied to convert airborne NO_2 maps to near-surface concentrations. A way forward could be combining airborne observations with a city-scale dispersion model that links NSCs and SCDs and also needs to consider 3D radiative transfer. The unique dataset collected in the MuNIC campaign will be important for validating such approaches.

We found that NO_x emission estimates of the two combined heat and power (CHP) plants are significantly higher than reported values, but uncertainties are high due to high variability in wind speeds during the campaign day. Wind speeds are required to compute the fluxes as well as plume rise, dispersion and residence time that have a large impact on the estimated emissions. The estimates are also likely overestimated, because the applied mass balance approaches assume steady-state conditions, which seems to be insufficient for convective conditions, if accurate and high-resolution wind fields are not available. Nonetheless, NO_x emission estimates for Munich South are consistent with CO_2 emissions determined from two ground-based FTIR instruments.

Due to the difficulty of estimating emission from airborne imaging spectrometers under convective conditions, flying during stable conditions, i.e. higher and less variable wind speeds and directions, should be an option to reduce uncertainties in future campaigns. While conditions tend to be less convective in the early morning and late afternoon, such conditions increase other challenges including large solar zenith angles, for which 3D radiative transfer effects can affect emission estimates (Schwaerzel et al., 2020). For the planning of future campaigns, it is therefore important to consider both illumination and wind conditions in order to obtain the best possible situation for measurements and data analyses.

Data availability. The data used in this publication are available at the supplement.

Author contributions. The paper was written by GK with input from all co-authors. The APEX measurements were coordinated by AH. The APEX Level-0, surface reflectance and auxiliary products were processed by AH. The APEX NO_2 product was retrieved and analysed by GK. The ASD measurements were conducted by AS, post-processed by AD, and analysed and compared to APEX by MS and GK. The CAPS measurement were analysed by GK. The CE-DOAS and LP-DOAS measurements were analysed by YZ, KLC and MW. The FTIR measurments were conducted, analysed and interpreted by JC, DHN and FD. The stationary MAX-DOAS measurements were analysed by KLC. The mobile MAX-DOAS measurements were conducted by SDo and SDö and analysed and interpreted by SDo, SDö and TW. The MAX-DOAS instrument at OvM was provided by CL. The analysis and comparison of the data, the computation of the NSC and VCD ratios and the estimation of the emissions was conducted by GK. The MuNIC campaign was organized by GK, DB and MW. The study was conducted within the HighNOCS project supervised by BB.

Competing interests. Some authors are members of the editorial board of Atmospheric Measurement Techniques. The peer-review process was guided by an independent editor, and the authors have also no other competing interests to declare.

Acknowledgements. We would like to thank Sebastian Böhnke and Markus Garhammer for their support in driving the vehicles, Nan Hao and Zhouru Wang for assistance with setting up the MAX-DOAS instruments, Katharina Hauk for the support with the measurements and analysis of the mobile MAX-DOAS data. We acknowledge the Bavarian State Office for the Environment (LfU) for providing the NO_2 measurements from the monitoring network, the Stadtwerke München (SWM) for providing operation data for the Munich South CHP plant, and MeteoSwiss for providing the COSMO-1 and COSMO-7 analysis product. We are very thankful to Ludwig Heinle for setting up the FTIR measurements, Frank Hase (KIT) for providing his EM27 instrument.

Financial support. The research has been supported by the Swiss National Science Foundation (SNSF) as part of the MuNIC and HighNOCS project (grant no. 170264 and 172533) as well as by Swiss University Conference and ETH board as part of the Swiss Earth Observatory Network (SEON).

References

Beelen, R., Raaschou-Nielsen, O., Stafoggia, M., Andersen, Z. J., Weinmayr, G., Hoffmann, B., Wolf, K., Samoli, E., Fischer, P., Nieuwen-huijsen, M., Vineis, P., Xun, W. W., Katsouyanni, K., Dimakopoulou, K., Oudin, A., Forsberg, B., Modig, L., Havulinna, A. S., Lanki, T., Turunen, A., Oftedal, B., Nystad, W., Nafstad, P., De Faire, U., Pedersen, N. L., Östenson, C.-G., Fratiglioni, L., Penell, J., Korek, M., Pershagen, G., Eriksen, K. T., Overvad, K., Ellermann, T., Eeftens, M., Peeters, P. H., Meliefste, K., Wang, M., Bueno-de Mesquita, B., Sugiri, D., Krämer, U., Heinrich, J., de Hoogh, K., Key, T., Peters, A., Hampel, R., Concin, H., Nagel, G., Ineichen, A., Schaffner, E., Probst-Hensch, N., Künzli, N., Schindler, C., Schikowski, T., Adam, M., Phuleria, H., Vilier, A., Clavel-Chapelon, F., Declercq, C., Grioni, S., Krogh, V., Tsai, M.-Y., Ricceri, F., Sacerdote, C., Galassi, C., Migliore, E., Ranzi, A., Cesaroni, G., Badaloni, C., Forastiere, F., Tamayo, I., Amiano, P., Dorronsoro, M., Katsoulis, M., Trichopoulou, A., Brunekreef, B., and Hoek, G.: Effects of long-term exposure to air pollution on natural-cause mortality: an analysis of 22 European cohorts within the multicentre ESCAPE project, The Lancet, 383, 785–795, https://doi.org/10.1016/S0140-6736(13)62158-3, http://dx.doi.org/10.1016/S0140-6736(13)62158-3, 2014.

Beirle, S., Boersma, K. F., Platt, U., Lawrence, M. G., and Wagner, T.: Megacity Emissions and Lifetimes of Nitrogen Oxides Probed from Space, Science, 333, 1737–1739, https://doi.org/10.1126/science.1207824, 2011.

Beirle, S., Borger, C., Dörner, S., Li, A., Hu, Z., Liu, F., Wang, Y., and Wagner, T.: Pinpointing nitrogen oxide emissions from space, Science Advances, 5, https://doi.org/10.1126/sciadv.aax9800, https://advances.sciencemag.org/content/5/11/eaax9800, 2019.

Berk, A., Anderson, G. P., Acharya, P. K., Bernstein, L. S., Muratov, L., Lee, J., Fox, M. J., Adler-Golden, S. M., Chetwynd, J. H., Hoke, M. L., Lockwood, R. B., Cooley, T. W., and Gardner, J. A.: MODTRAN5: a reformulated atmospheric band model with auxiliary species and practical multiple scattering options, in: Multispectral and Hyperspectral Remote Sensing Instruments and Applications II, edited by Larar, A. M., Suzuki, M., and Tong, Q., vol. 5655, pp. 88 – 95, International Society for Optics and Photonics, SPIE, https://doi.org/10.1117/12.578758, 2005.

Bigi, A., Mueller, M., Grange, S. K., Ghermandi, G., and Hueglin, C.: Performance of NO, NO_2 low cost sensors and three calibration approaches within a real world application, Atmospheric Measurement Techniques, 11, 3717–3735, https://doi.org/10.5194/amt-11-3717-2018, https://amt.copernicus.org/articles/11/3717/2018/, 2018.

Boersma, K. F., Eskes, H. J., Dirksen, R. J., van der A, R. J., Veefkind, J. P., Stammes, P., Huijnen, V., Kleipool, Q. L., Sneep, M., Claas, J., Leitão, J., Richter, A., Zhou, Y., and Brunner, D.: An improved tropospheric NO2 column retrieval algorithm for the Ozone Monitoring Instrument, Atmospheric Measurement Techniques, 4, 1905–1928, https://doi.org/10.5194/amt-4-1905-2011, http://www.atmos-meas-tech.net/4/1905/2011/, 2011.

Brunekreef, B. and Holgate, S. T.: Air pollution and health, Lancet, 360, 1233–1242, https://doi.org/10.1016/s0140-6736(02)11274-8, <GotoISI>://WOS:000178708100030, 2002.

Chan, K. L., Wiegner, M., Wenig, M., and Pöhler, D.: Observations of tropospheric aerosols and NO_2 in Hong Kong over 5 years using ground based MAX-DOAS, Science of The Total Environment, 619-620, 1545 – 1556, https://doi.org/10.1016/j.scitotenv.2017.10.153, 2018.

Chan, K. L., Wang, Z., Ding, A., Heue, K.-P., Shen, Y., Wang, J., Zhang, F., Shi, Y., Hao, N., and Wenig, M.: MAX-DOAS measurements of tropospheric NO_2 and HCHO in Nanjing and a comparison to ozone monitoring instrument observations, Atmospheric Chemistry and Physics, 19, 10051–10071, https://doi.org/10.5194/acp-19-10051-2019, 2019.

630 Chan, K. L., Wiegner, M., van Geffen, J., De Smedt, I., Alberti, C., Cheng, Z., Ye, S., and Wenig, M.: MAX-DOAS measurements of tropospheric NO_2 and HCHO in Munich and the comparison to OMI and TROPOMI satellite observations, Atmospheric Measurement Techniques, 13, 4499–4520, https://doi.org/10.5194/amt-13-4499-2020, https://amt.copernicus.org/articles/13/4499/2020/, 2020.

Chen, J., Viatte, C., Hedelius, J. K., Jones, T., Franklin, J. E., Parker, H., Gottlieb, E. W., Wennberg, P. O., Dubey, M. K., and Wofsy, S. C.: Differential column measurements using compact solar-tracking spectrometers, Atmospheric Chemistry and Physics, 16, 8479–8498, 635 https://doi.org/10.5194/acp-16-8479-2016, 2016.

Chen, J., Nguyen, H., Toja-Silva, F., Heinle, L., Hase, F., and Butz, A.: Power Plant Emission Monitoring in Munich Using Differential Column Measurements, EGU General Assembly 2017, vol. 19, EGU2017-16423, https://doi.org/10.13140/RG.2.2.31907.30247, 2017.

de Hoogh, K., Saucy, A., Shtein, A., Schwartz, J., West, E. A., Strassmann, A., Puhan, M., Röösli, M., Stafoggia, M., and Kloog, I.: Predicting Fine-Scale Daily NO2 for 2005–2016 Incorporating OMI Satellite Data Across Switzerland, Environmental Science & Technology, 53, 640 10 279–10 287, https://doi.org/10.1021/acs.est.9b03107, 2019.

Dietrich, F., Chen, J., Voggenreiter, B., Aigner, P., Nachtigall, N., and Reger, B.: MUCCnet: Munich Urban Carbon Column network, Atmospheric Measurement Techniques, 14, 1111–1126, https://doi.org/10.5194/amt-14-1111-2021, 2021.

Emde, C., Buras-Schnell, R., Kylling, A., Mayer, B., Gasteiger, J., Hamann, U., Kylling, J., Richter, B., Pause, C., Dowling, T., and Bugliaro, L.: The libRadtran software package for radiative transfer calculations (version 2.0.1), Geoscientific Model Development, 9, 1647–1672, 645 https://doi.org/10.5194/gmd-9-1647-2016, 2016.

European Environment Agency: Air quality in Europe-2019 Report, Tech. rep., https://www.eea.europa.eu/publications/air-quality-in-europe-2019, 2019.

European Environment Agency: European Industrial Emission Portal, availble at https://industry.eea.europa.eu/, last access: 23 June 2021, 2021.

650 Gisi, M., Hase, F., Dohe, S., Blumenstock, T., Simon, A., and Keens, A.: XCO_2-measurements with a tabletop FTS using solar absorption spectroscopy, Atmospheric Measurement Techniques, 5, 2969–2980, https://doi.org/10.5194/amt-5-2969-2012, 2012.

Hagemann, R., Corsmeier, U., Kottmeier, C., Rinke, R., Wieser, A., and Vogel, B.: Spatial variability of particle number concentrations and NO_x in the Karlsruhe (Germany) area obtained with the mobile laboratory 'AERO-TRAM', Atmospheric Environment, 94, 341–352, https://doi.org/https://doi.org/10.1016/j.atmosenv.2014.05.051, 2014.

655 Hase, F., Frey, M., Blumenstock, T., Groß, J., Kiel, M., Kohlhepp, R., Mengistu Tsidu, G., Schäfer, K., Sha, M. K., and Orphal, J.: Application of portable FTIR spectrometers for detecting greenhouse gas emissions of the major city Berlin, Atmospheric Measurement Techniques, 8, 3059–3068, https://doi.org/10.5194/amt-8-3059-2015, 2015.

Hedelius, J. K., Viatte, C., Wunch, D., Roehl, C. M., Toon, G. C., Chen, J., Jones, T., Wofsy, S. C., Franklin, J. E., Parker, H., Dubey, M. K., and Wennberg, P. O.: Assessment of errors and biases in retrievals of X_{CO_2}, X_{CH_4}, X_{CO}, and X_{N_2O} from a $0.5\,cm^{-1}$ resolution 660 solar-viewing spectrometer, Atmospheric Measurement Techniques, 9, 3527–3546, https://doi.org/10.5194/amt-9-3527-2016, 2016.

Heimann, I., Bright, V. B., McLeod, M. W., Mead, M. I., Popoola, O. A. M., Stewart, G. B., and Jones, R. L.: Source attribution of air pollution by spatial scale separation using high spatial density networks of low cost air quality sensors, Atmospheric Environment, 113, 10–19, https://doi.org/10.1016/j.atmosenv.2015.04.057, http://www.sciencedirect.com/science/article/pii/S1352231015300583, 2015.

Heue, K. P., Wagner, T., Broccardo, S. P., Walter, D., Piketh, S. J., Ross, K. E., Beirle, S., and Platt, U.: Direct observation of two di-665 mensional trace gas distributions with an airborne Imaging DOAS instrument, Atmospheric Chemistry and Physics, 8, 6707–6717, https://doi.org/10.5194/acp-8-6707-2008, http://www.atmos-chem-phys.net/8/6707/2008/, 2008.

Hueni, A., Biesemans, J., Meuleman, K., Dell'Endice, F., Schlapfer, D., Odermatt, D., Kneubuehler, M., Adriaensen, S., Kempenaers, S., Nieke, J., and Itten, K. I.: Structure, Components, and Interfaces of the Airborne Prism Experiment (APEX) Processing and Archiving Facility, IEEE Transactions on Geoscience and Remote Sensing, 47, 29–43, https://doi.org/10.1109/TGRS.2008.2005828, 2009.

670 Hueni, A., Lenhard, K., Baumgartner, A., and Schaepman, M. E.: Airborne Prism Experiment Calibration Information System, IEEE Transactions on Geoscience and Remote Sensing, 51, 5169–5180, https://doi.org/10.1109/TGRS.2013.2246575, 2013.

Hundt, P. M., Müller, M., Mangold, M., Tuzson, B., Scheidegger, P., Looser, H., Hüglin, C., and Emmenegger, L.: Mid-IR spectrometer for mobile, real-time urban NO_2 measurements, Atmospheric Measurement Techniques, 11, 2669–2681, https://doi.org/10.5194/amt-11-2669-2018, https://amt.copernicus.org/articles/11/2669/2018/, 2018.

675 Ibrahim, O., Shaiganfar, R., Sinreich, R., Stein, T., Platt, U., and Wagner, T.: Car MAX-DOAS measurements around entire cities: quantification of NO_x emissions from the cities of Mannheim and Ludwigshafen (Germany), Atmospheric Measurement Techniques, 3, 709–721, https://doi.org/10.5194/amt-3-709-2010, 2010.

Irie, H., Takashima, H., Kanaya, Y., Boersma, K. F., Gast, L., Wittrock, F., Brunner, D., Zhou, Y., and Van Roozendael, M.: Eight-component retrievals from ground-based MAX-DOAS observations, Atmospheric Measurement Techniques, 4, 1027–1044, 680 https://doi.org/10.5194/amt-4-1027-2011, http://www.atmos-meas-tech.net/4/1027/2011/, 2011.

Karagulian, F., Barbiere, M., Kotsev, A., Spinelle, L., Gerboles, M., Lagler, F., Redon, N., Crunaire, S., and Borowiak, A.: Review of the Performance of Low-Cost Sensors for Air Quality Monitoring, Atmosphere, 10, https://doi.org/10.3390/atmos10090506, https://www.mdpi.com/2073-4433/10/9/506, 2019.

Kebabian, P. L., Herndon, S. C., and Freedman, A.: Detection of Nitrogen Dioxide by Cavity Attenuated Phase Shift Spectroscopy, Analytical 685 Chemistry, 77, 724–728, https://doi.org/10.1021/ac048715y, pMID: 15649079, 2005.

Kebabian, P. L., Wood, E. C., Herndon, S. C., and Freedman, A.: A Practical Alternative to Chemiluminescence-Based Detection of Nitrogen Dioxide: Cavity Attenuated Phase Shift Spectroscopy, Environmental Science & Technology, 42, 6040–6045, https://doi.org/10.1021/es703204j, pMID: 18767663, 2008.

Kim, M., Brunner, D., and Kuhlmann, G.: Importance of satellite observations for high-resolution mapping of near-surface NO2 by ma-690 chine learning, Remote Sensing of Environment, 264, 112 573, https://doi.org/https://doi.org/10.1016/j.rse.2021.112573, https://www.sciencedirect.com/science/article/pii/S0034425721002935, 2021.

Kreher, K., Van Roozendael, M., Hendrick, F., Apituley, A., Dimitropoulou, E., Frieß, U., Richter, A., Wagner, T., Lampel, J., Abuhassan, N., Ang, L., Anguas, M., Bais, A., Benavent, N., Bösch, T., Bognar, K., Borovski, A., Bruchkouski, I., Cede, A., Chan, K. L., Donner, S., Drosoglou, T., Fayt, C., Finkenzeller, H., Garcia-Nieto, D., Gielen, C., Gómez-Martín, L., Hao, N., Henzing, B., Herman, J. R., Hermans, 695 C., Hoque, S., Irie, H., Jin, J., Johnston, P., Khayyam Butt, J., Khokhar, F., Koenig, T. K., Kuhn, J., Kumar, V., Liu, C., Ma, J., Merlaud, A., Mishra, A. K., Müller, M., Navarro-Comas, M., Ostendorf, M., Pazmino, A., Peters, E., Pinardi, G., Pinharanda, M., Piters, A., Platt, U., Postylyakov, O., Prados-Roman, C., Puentedura, O., Querel, R., Saiz-Lopez, A., Schönhardt, A., Schreier, S. F., Seyler, A., Sinha, V., Spinei, E., Strong, K., Tack, F., Tian, X., Tiefengraber, M., Tirpitz, J.-L., van Gent, J., Volkamer, R., Vrekoussis, M., Wang, S., Wang, Z., Wenig, M., Wittrock, F., Xie, P. H., Xu, J., Yela, M., Zhang, C., and Zhao, X.: Intercomparison of NO$_2$, O$_4$, O$_3$ and HCHO slant column 700 measurements by MAX-DOAS and zenith-sky UV–visible spectrometers during CINDI-2, Atmospheric Measurement Techniques, 13, 2169–2208, https://doi.org/10.5194/amt-13-2169-2020, 2020.

Kuhlmann, G.: Data-driven emission quantification (Python package), available at https://gitlab.com/empa503/remote-sensing/ddeq, 2021a.

Kuhlmann, G.: flexDOAS – A flexible Python library for DOAS analysis, https://gitlab.com/empa503/remote-sensing/flexdoas, last access: January 7, 2022, 2021b.

705 Kuhlmann, G.: OMI/TROPOMI gridding algorithm, https://gitlab.com/empa503/remote-sensing/gridding-algorithm, last access: January 7, 2022, 2021c.

Kuhlmann, G., Hartl, A., Cheung, H. M., Lam, Y. F., and Wenig, M. O.: A novel gridding algorithm to create regional trace gas maps from satellite observations, Atmos. Meas. Tech., 7, 451–467, https://doi.org/10.5194/amt-7-451-2014, http://www.atmos-meas-tech.net/7/451/2014/, 2014.

710 Kuhlmann, G., Hueni, A., Damm, A., and Brunner, D.: An Algorithm for In-Flight Spectral Calibration of Imaging Spectrometers, Remote Sensing, 8, 1017, https://doi.org/10.3390/rs8121017, 2016.

Kuhlmann, G., Broquet, G., Marshall, J., Clément, V., Löscher, A., Meijer, Y., and Brunner, D.: Detectability of CO_2 emission plumes of cities and power plants with the Copernicus Anthropogenic CO_2 Monitoring (CO2M) mission, Atmospheric Measurement Techniques, 12, 6695–6719, https://doi.org/10.5194/amt-12-6695-2019, https://amt.copernicus.org/articles/12/6695/2019/, 2019.

715 Kuhlmann, G., Henne, S., Meijer, Y., and Brunner, D.: Quantifying CO_2 Emissions of Power Plants With CO_2 and NO_2 Imaging Satellites, Frontiers in Remote Sensing, 2, 14, https://doi.org/10.3389/frsen.2021.689838, https://www.frontiersin.org/article/10.3389/frsen.2021.689838, 2021.

Lawrence, J. P., Anand, J. S., Vande Hey, J. D., White, J., Leigh, R. R., Monks, P. S., and Leigh, R. J.: High-resolution measurements from the airborne Atmospheric Nitrogen Dioxide Imager (ANDI), Atmospheric Measurement Techniques, 8, 4735–4754,
720 https://doi.org/10.5194/amt-8-4735-2015, http://www.atmos-meas-tech.net/8/4735/2015/, 2015.

Leigh, R. J., Corlett, G. K., Frieß, U., and Monks, P. S.: Spatially resolved measurements of nitrogen dioxide in an urban environment using concurrent multi-axis differential optical absorption spectroscopy, Atmospheric Chemistry and Physics, 7, 4751–4762, https://doi.org/10.5194/acp-7-4751-2007, https://acp.copernicus.org/articles/7/4751/2007/, 2007.

Lorente, A., Boersma, K., Eskes, H., Veefkind, J., Van Geffen, J., de Zeeuw, M., van der Gon, H. D., Beirle, S., and Krol, M.:
725 Quantification of nitrogen oxides emissions from build-up of pollution over Paris with TROPOMI, Scientific Reports, 9, 1–10, https://doi.org/10.1038/s41598-019-56428-5, 2019.

Maiheu, B., Lefebvre, W., Walton, H., Dajnak, D., Janssen, S., Williams, M., Blyth, L., and Beevers, S.: Improved Methodologies for NO2 Exposure Assessment in the EU, Study accomplished under the authority of the European Commission, DG-Environment under service contract 070201/2015/SER/717473/C.3, Final report, Report, 2017.

730 Mayer, B. and Kylling, A.: Technical note: The libRadtran software package for radiative transfer calculations - description and examples of use, Atmospheric Chemistry and Physics, 5, 1855–1877, 2005.

Mueller, M., Wagner, M., Barmpadimos, I., and Hueglin, C.: Two-week NO2 maps for the City of Zurich, Switzerland, derived by statistical modelling utilizing data from a routine passive diffusion sampler network, Atmospheric Environment, 106, 1–10, 2015.

Nowlan, C. R., Liu, X., Leitch, J. W., Chance, K., González Abad, G., Liu, C., Zoogman, P., Cole, J., Delker, T., Good, W., Murcray, F.,
735 Ruppert, L., Soo, D., Follette-Cook, M. B., Janz, S. J., Kowalewski, M. G., Loughner, C. P., Pickering, K. E., Herman, J. R., Beaver, M. R., Long, R. W., Szykman, J. J., Judd, L. M., Kelley, P., Luke, W. T., Ren, X., and Al-Saadi, J. A.: Nitrogen dioxide observations from the Geostationary Trace gas and Aerosol Sensor Optimization (GeoTASO) airborne instrument: Retrieval algorithm and measurements during DISCOVER-AQ Texas 2013, Atmospheric Measurement Techniques, 9, 2647–2668, https://doi.org/10.5194/amt-9-2647-2016, http://www.atmos-meas-tech.net/9/2647/2016/, 2016.

740 Platt, U., Heue, K.-P., and Pöhler, D.: Two-and Three Dimensional Observation of Trace Gas and Aerosol Distributions by DOAS Techniques, in: Atmospheric and Biological environmental monitoring, pp. 3–11, Springer, 2009.

Popp, C., Brunner, D., Damm, A., Van Roozendael, M., Fayt, C., and Buchmann, B.: High-resolution NO2 remote sensing from the Airborne Prism EXperiment (APEX) imaging spectrometer, Atmospheric Measurement Techniques, 5, 2211–2225, https://doi.org/10.5194/amt-5-2211-2012, http://www.atmos-meas-tech.net/5/2211/2012/, 2012.

745 Richter, R. and Schläpfer, D.: Geo-atmospheric processing of airborne imaging spectrometry data. Part 2: Atmospheric/topographic correction, International Journal of Remote Sensing, 23, 2631–2649, https://doi.org/10.1080/01431160110115834, 2002.

Rodgers, C. D.: Inverse methods for atmospheric sounding: theory and practice, World Scientific Publishing, 2000.

Schaepman, M. E., Jehle, M., Hueni, A., D'Odorico, P., Damm, A., Weyermann, J., Schneider, F. D., Laurent, V., Popp, C., Seidel, F. C., Lenhard, K., Gege, P., Küchler, C., Brazile, J., Kohler, P., De Vos, L., Meuleman, K., Meynart, R., Schläpfer, D., Kneubühler, M., and

750 Itten, K. I.: Advanced radiometry measurements and Earth science applications with the Airborne Prism Experiment (APEX), Remote Sensing of Environment, 158, 207–219, https://doi.org/https://doi.org/10.1016/j.rse.2014.11.014, https://www.sciencedirect.com/science/article/pii/S0034425714004568, 2015.

Schaepman-Strub, G., Schaepman, M., Painter, T., Dangel, S., and Martonchik, J.: Reflectance quantities in optical remote sensing—definitions and case studies, Remote Sensing of Environment, 103, 27–42, https://doi.org/https://doi.org/10.1016/j.rse.2006.03.002,

755 2006.

Schönhardt, A., Altube, P., Gerilowski, K., Krautwurst, S., Hartmann, J., Meier, A. C., Richter, A., and Burrows, J. P.: A wide field-of-view imaging DOAS instrument for two-dimensional trace gas mapping from aircraft, Atmospheric Measurement Techniques, 8, 5113–5131, https://doi.org/10.5194/amt-8-5113-2015, http://www.atmos-meas-tech.net/8/5113/2015/, 2015.

Schwaerzel, M., Emde, C., Brunner, D., Morales, R., Wagner, T., Berne, A., Buchmann, B., and Kuhlmann, G.: Three-dimensional radiative

760 transfer effects on airborne, satellite and ground-based trace gas remote sensing, Atmos. Meas. Tech., https://doi.org/10.5194/amt-2020-146, 2020.

Schwaerzel, M., Brunner, D., Jakub, F., Emde, C., Buchmann, B., Berne, A., and Kuhlmann, G.: Impact of 3D radiative transfer on airborne NO_2 imaging remote sensing over cities with buildings, Atmos. Meas. Tech. Discuss., 2021.

Shaiganfar, R., Beirle, S., Sharma, M., Chauhan, A., Singh, R. P., and Wagner, T.: Estimation of NO_x emissions from Delhi using

765 Car MAX-DOAS observations and comparison with OMI satellite data, Atmospheric Chemistry and Physics, 11, 10 871–10 887, https://doi.org/10.5194/acp-11-10871-2011, 2011.

Tack, F., Merlaud, A., Iordache, M.-D., Danckaert, T., Yu, H., Fayt, C., Meuleman, K., Deutsch, F., Fierens, F., and Van Roozendael, M.: High-resolution mapping of the NO_2 spatial distribution over Belgian urban areas based on airborne APEX remote sensing, Atmospheric Measurement Techniques, 10, 1665–1688, https://doi.org/10.5194/amt-10-1665-2017, https://amt.copernicus.org/articles/10/1665/2017/,

770 2017.

Tack, F., Merlaud, A., Meier, A. C., Vlemmix, T., Ruhtz, T., Iordache, M.-D., Ge, X., van der Wal, L., Schuettemeyer, D., Ardelean, M., Calcan, A., Constantin, D., Schönhardt, A., Meuleman, K., Richter, A., and Van Roozendael, M.: Intercomparison of four airborne imaging DOAS systems for tropospheric NO_2 mapping – the AROMAPEX campaign, Atmospheric Measurement Techniques, 12, 211–236, https://doi.org/10.5194/amt-12-211-2019, 2019.

775 Toja-Silva, F., Chen, J., Hachinger, S., and Hase, F.: CFD simulation of CO2 dispersion from urban thermal power plant: Analysis of turbulent Schmidt number and comparison with Gaussian plume model and measurements, Journal of Wind Engineering and Industrial Aerodynamics, 169, 177–193, https://doi.org/https://doi.org/10.1016/j.jweia.2017.07.015, https://www.sciencedirect.com/science/article/pii/S0167610517302258, 2017.

U.S. EPA: Greenhouse Gas Inventory Guidance - Direct Emissions from Stationary Combustion Sources, Tech. rep., https://www.epa.gov/sites/default/files/2016-03/documents/stationaryemissions_3_2016.pdf, 2016.

VDI - Fachbereich Umweltmeteorologie: Dispersion of air pollutants in the atmosphere; determination of plume rise, Tech. Rep. VDI 3782 Blatt 3, VDI/DIN-Kommission Reinhaltung der Luft (KRdL) - Normenausschuss, 1985.

VDI - Fachbereich Umweltmeteorologie: Atmospheric dispersion models; Gaussian plume model for the determination of ambient air characteristics, Tech. Rep. VDI 3782 Blatt 1, VDI/DIN-Kommission Reinhaltung der Luft (KRdL) - Normenausschuss, 2009.

Virtanen, P., Gommers, R., Oliphant, T. E., Haberland, M., Reddy, T., Cournapeau, D., Burovski, E., Peterson, P., Weckesser, W., Bright, J., van der Walt, S. J., Brett, M., Wilson, J., Millman, K. J., Mayorov, N., Nelson, A. R. J., Jones, E., Kern, R., Larson, E., Carey, C. J., Polat, İ., Feng, Y., Moore, E. W., VanderPlas, J., Laxalde, D., Perktold, J., Cimrman, R., Henriksen, I., Quintero, E. A., Harris, C. R., Archibald, A. M., Ribeiro, A. H., Pedregosa, F., van Mulbregt, P., and SciPy 1.0 Contributors: SciPy 1.0: Fundamental Algorithms for Scientific Computing in Python, Nature Methods, 17, 261–272, https://doi.org/10.1038/s41592-019-0686-2, 2020.

Wagner, T., Deutschmann, T., and Platt, U.: Determination of aerosol properties from MAX-DOAS observations of the Ring effect, Atmospheric Measurement Techniques, 2, 495–512, https://doi.org/10.5194/amt-2-495-2009, 2009.

Wagner, T., Ibrahim, O., Shaiganfar, R., and Platt, U.: Mobile MAX-DOAS observations of tropospheric trace gases, Atmospheric Measurement Techniques, 3, 129–140, https://doi.org/10.5194/amt-3-129-2010, 2010.

World Health Organization: WHO global air quality guidelines: particulate matter (PM2.5 and PM10), ozone, nitrogen dioxide, sulfur dioxide and carbon monoxide, World Health Organization, https://apps.who.int/iris/handle/10665/345329, 2021.

Xu, H., Bechle, M. J., Wang, M., Szpiro, A. A., Vedal, S., Bai, Y., and Marshall, J. D.: National PM2.5 and NO2 Exposure Models for China Based on Land Use Regression, Satellite Measurements, and Universal Kriging, 655, 423–433, https://doi.org/10.1016/j.scitotenv.2018.11.125, http://www.sciencedirect.com/science/article/pii/S0048969718344802.

Zhao, X., Marshall, J., Hachinger, S., Gerbig, C., Frey, M., Hase, F., and Chen, J.: Analysis of total column CO_2 and CH_4 measurements in Berlin with WRF-GHG, Atmospheric Chemistry and Physics, 19, 11 279–11 302, https://doi.org/10.5194/acp-19-11279-2019, 2019.

Zhu, Y., Chen, J., Bi, X., Kuhlmann, G., Chan, K. L., Dietrich, F., Brunner, D., Ye, S., and Wenig, M.: Spatial and temporal representativeness of point measurements for nitrogen dioxide pollution levels in cities, Atmospheric Chemistry and Physics, 20, 13 241–13 251, https://doi.org/10.5194/acp-20-13241-2020, 2020.